Crystallization of Interstitial Liquid and Latent Heat Buffering in Solidifying Gabbros: Skaergaard Intrusion, Greenland

OLIVIER NAMUR[1]*, MADELEINE C. S. HUMPHREYS[2]† AND MARIAN B. HOLNESS[1]

[1]DEPARTMENT OF EARTH SCIENCES, UNIVERSITY OF CAMBRIDGE, DOWNING STREET, CAMBRIDGE CB2 3EQ, UK

[2]DEPARTMENT OF EARTH SCIENCES, UNIVERSITY OF OXFORD, SOUTH PARKS ROAD, OXFORD OX1 3AN, UK

New compositional profiles across plagioclase grains from the Layered Series (LS), Marginal Border Series (MBS) and Upper Border Series (UBS) of the Skaergaard intrusion are used to understand the mechanisms of cumulate rock solidification and the fate of the interstitial liquid. The data show that plagioclase crystals display three types of compositional profile over the whole intrusion, as follows. (1) Grains with normal zoning, which dominate the MBS and UBS. These are interpreted as having formed at the top of a crystal mush and then buried in the cumulate pile. Crystallization of the interstitial melt resulted in liquid differentiation and produced normally zoned rims on plagioclase cores. (2) Unzoned crystals, which dominate the upper part of the LS, also crystallized at the top of the mush and were then buried in mush with a low interstitial liquid fraction or one experiencing convective movements that kept the liquid to a constant composition. (3) Crystals with a mantle of decreasing An content followed by a rim of constant composition. Grains showing this complex zoning mostly occur in the lower parts of the LS. Depending on the stratigraphic position within the intrusion, the composition of the rim can be An_{56}, An_{51} or An_{40}. In the main magma body, these compositions (An contents) correspond to those of plagioclase primocrysts (e.g. cores) at the appearance of cumulus clinopyroxene (An_{56}), Fe–Ti oxides (An_{51}) and apatite (An_{40}). Compositional buffering of plagioclase rims is interpreted as being a consequence of enhanced release of latent heat of crystallization at the appearance of new interstitial phases in the crystal mush. When a new phase saturates, the latent heat contribution to the global enthalpy budget of the system becomes sufficiently high to keep the interstitial melt at its liquidus temperature for a period of time that could exceed thousands of years. Under these conditions, equilibrium, adcumulus growth together with diffusion and possibly advection of chemical components result in the formation of plagioclase rims of constant composition (An content). Efficient thermal buffering of the mush liquid depends on the porosity (i.e. fraction of liquid within the mush) and the degree of compositional homogeneity of the mush. In a heterogeneous and highly porous mush, saturation of the new phase occurs in the coldest part of the mush and the enhanced latent heat release at the saturation of this phase is quickly dissipated to the whole volume of liquid, including the warmest part that is not yet saturated in a new phase. As a consequence, no thermal buffering occurs and interstitial crystallization produces grains with normal zoning. The distribution of the various types of plagioclase grains throughout the Skaergaard intrusion can therefore be used to infer the spatial variability in the physical properties of the crystal mush, such as the residual porosity, both at an intrusion-wide scale and at a millimetre- to centimetre-scale.

KEY WORDS: *plagioclase; thermal buffering; thermodynamics; zoning; cumulate; layered intrusion; Skaergaard*

INTRODUCTION

Formation of cumulate rocks starts with the nucleation and growth of liquidus crystals (primocrysts), which are then captured in a crystal mush. When a new phase saturates in the mush liquid, it may form only a few nuclei on which further growth results in the formation of large poikilitic grains locally enclosing the primocrysts. In gabbroic

*Corresponding author. Present address: Institute of Mineralogy, University of Hannover, Callinstrasse 3, 30167 Hannover, Germany. Telephone: +44 (0) 1223 333400. Fax: +44 (0) 1223 333450. E-mail: obn21@cam.ac.uk

†Present address: Department of Earth Sciences, University of Durham, Science Labs, Durham DH1 3LE, UK

rocks this is especially evident for pyroxenes (clinopyroxene and orthopyroxene) and for Fe–Ti oxides (Wager *et al.*, 1960; McBirney & Hunter, 1995; Holness *et al.*, 2007; Namur *et al.*, 2010). Depending on the amount of interstitial material in cumulate rocks, cumulates may be classified into three end-member types: adcumulate with less than 7% of interstitial material, mesocumulate with 7–25% of interstitial material and orthocumulate with >25% of interstitial material (Wager *et al.*, 1960). The initial porosity of a cumulate rock is estimated to be in the range 40–60 vol. % (Irvine, 1980; Shirley, 1986; Philpotts *et al.*, 1998; Jerram *et al.*, 2003), which is significantly higher than the proportion calculated from the bulk chemistry of the interstitial material in most cumulates (e.g. Tegner *et al.*, 2009; Namur & Charlier, 2012). It is therefore evident that at least some interstitial liquid is mobile during the solidification of the crystal mush. Estimating the physical behaviour (i.e. mobility) of the interstitial melt upon cooling is, however, hampered by the lack of accurate constraints on some fundamental physical properties of the crystal matrix (e.g. viscosity), the thickness of the crystal mush and the rate of crystal accumulation at the top of the crystal mush (Kerr & Tait, 1986; Namur & Charlier, 2012).

A way to place constraints on the behaviour of the interstitial liquid within the crystal mush is to investigate the composition of the interstitial phases in cumulate rocks. However, very little consideration has been given to such interstitial phases in the past (e.g. Meurer & Claeson, 2002; Toplis *et al.*, 2008; Humphreys, 2009, 2011; Holness *et al.*, 2011; Namur & Charlier, 2012), probably because they generally equilibrate quickly with the continuously evolving interstitial melt. Their composition therefore does not help in deciphering the entire evolution of the melt. However, better constraints can be obtained from chemical zoning in plagioclase as this is not significantly altered by subsolidus diffusion on the time-scale of solidification, at least for the CaAl-NaSi exchange (e.g. An-content; Grove *et al.*, 1984).

If the mush liquid follows the same differentiation path as that of the main magma body (Meurer & Claeson, 2002), intra-grain chemical variations will be identical to those observed in primocryst cores from the level of primocryst accumulation to the top of the cumulate pile (Humphreys, 2009, 2011). However, processes such as physical compaction of the crystal mush (McKenzie, 1984, 2011; Tegner *et al.*, 2009), compositionally driven convection (Tait *et al.*, 1984; Toplis *et al.*, 2008) or separation of Fe-rich and Si-rich immiscible melts (Holness *et al.*, 2011; Humphreys, 2011) may also affect the composition, abundance, and evolution of interstitial mush liquid. Such processes involving the migration of interstitial liquid may produce grains with normal or reverse zoning in meso- to orthocumulates, or unzoned grains in adcumulates (Toplis *et al.*, 2008; Humphreys, 2009; Morse, 2012).

In this study, we present a new and comprehensive set of plagioclase major element compositions in Skaergaard samples from the floor, roof and wall cumulates. These samples are characterized by various liquidus assemblages and a range of crystallized interstitial liquid fractions. We describe three types of plagioclase grains: normally zoned, unzoned and with rims buffered to constant anorthite compositions. Plagioclase grains with normal zoning are interpreted as resulting from normal differentiation of the interstitial melt [i.e. orthocumulus growth according to the model of Wager *et al.* (1960)] and unzoned plagioclase grains are interpreted as having formed in a crystal mush depleted in mush liquid or during convective movements of liquid [i.e. they correspond to adcumulus growth according to the model of Wager *et al.* (1960)]. However, the growth of rims buffered to a constant composition in the third type of plagioclase grains cannot be explained by these processes. We demonstrate that the previously neglected process of thermal buffering, caused by peaks in latent heat released by the crystallization of new liquidus phases (Holness *et al.*, 2007; Morse, 2011), is critically important in controlling the solidification of the crystal mush. Thermal buffering, coupled with chemical diffusion of chemical species in the liquid phase, results in efficient adcumulus growth of thick rims of constant composition on plagioclase primocrysts. Our novel observations link compositional zoning in plagioclase grains to the enthalpy budget of fractionating magma in a layered intrusion, providing a link between the products of crystallization and the evolution of the physical properties of the mushy layer during solidification.

The mineral zoning patterns we describe are also observed in other layered intrusions (Meurer & Boudreau, 1996; Namur & Charlier, 2012) and in crystal mush fragments carried by erupted lavas (Hansen & Gronvold, 2000; Costa *et al.*, 2012), indicating that the thermal buffering process may be of general significance during solidification of any crystal mush, and may have important general implications for reconstructing fractionation and differentiation paths in mushes and magma chambers.

THE SKAERGAARD LAYERED INTRUSION

The Eocene Skaergaard intrusion of East Greenland occupies a box-shaped, fault-bounded chamber, approximately 8 km × 11 km × 4 km (Nielsen, 2004), at the contact between Precambrian gneisses and a thick overlying sequence of Eocene plateau lavas (Fig. 1a). The intrusion is divided into three main units: the Layered Series (LS), which crystallized on the floor, the Upper Border Series (UBS), which crystallized from the roof, and the Marginal Border Series (MBS), which grew inwards from the vertical walls (Fig. 1b). The Skaergaard intrusion crystallized from a single, homogeneous, convecting magma
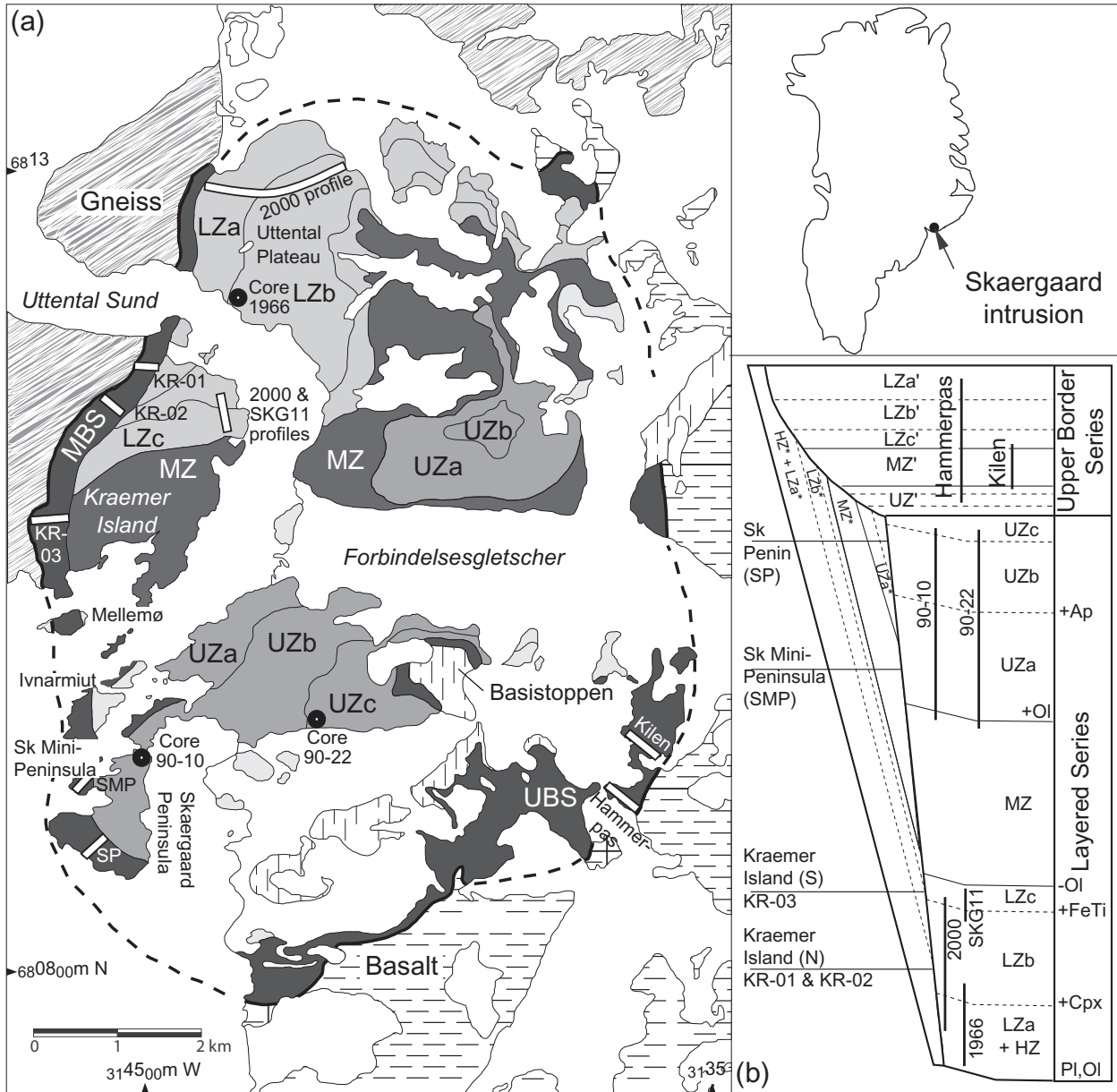
Fig. 1. (a) Simplified geological map of the Skaergaard intrusion showing the locations of the sampling traverses (SP, Skaergaard Peninsula; SMP, Skaergaard Mini-Peninsula; KR-0l, KR-02, KR-03, Kraemer Island) and drill cores investigated for this study. LZ, Lower Zone; MZ, Middle Zone; UZ, Upper Zone; MBS, Marginal Border Series; UBS, Upper Border Series. Map in the upper right corner shows the location of the map area in Greenland. (b) Schematic cross-section of the Skaergaard intrusion modified from Wager & Brown (1968) showing the spatial relationships between the Layered Series, Upper Border Series and Marginal Border Series. Subdivisions of each series and sequence of crystallization in the Layered Series are also shown. *, Notation of the zones and sub-zones of the MBS; ', notation of the zones and sub-zones of the UBS.

body and the three series (LS, MBS, US) crystallized simultaneously. These series follow roughly parallel trends of differentiation into the centre of the intrusion, converging at the Sandwich Horizon (Wager & Deer, 1939; Hoover, 1989a; Salmonsen & Tegner, 2013). This is confirmed by the identical An content of plagioclase at the appearance of any cumulus phase in the three series (Hoover, 1989a;

Thy *et al.*, 2009a; Salmonsen & Tegner, 2013). The composition of other phases such as olivine and clinopyroxene cannot so easily be used to compare the three series because these minerals equilibrate rapidly with the interstitial melt.

The stratigraphy of the Layered Series is subdivided, based on changes in the primocryst assemblage, into

plagioclase + olivine (Hidden Zone, HZ and Lower Zone A, LZa); plag + ol + augite (LZb); plag + ol + aug + Fe–Ti oxides (LZc); plag + aug + ox (+ pigeonite immediately afterwards; Middle Zone, MZ); plag + ol + aug + ox (Upper Zone A, UZa); plag + ol + aug + ox + apatite (UZb); plag + ol + aug + ox + ap + ferro-hedenbergite (inverted from β-ferrobustamite; UZc), where plag is plagioclase, ol is olivine, aug is augite, ox is Fe–Ti oxides, ap is apatite (Fig. 1b). Continuous fractional crystallization is also recorded by the compositions of the primocryst minerals, which change systematically with increasing stratigraphic height (plagioclase: $An_{72–29}$, Maaloe, 1976; Tegner, 1997; Jang & Naslund, 2001; Tegner & Cawthorn, 2010; Morse, 2012; olivine: $Fo_{70–0}$; clinopyroxene $Mg\#_{77–0}$; Wager & Brown, 1968; McBirney, 1989; Thy et al., 2009a).

The Marginal Border Series is subdivided in an analogous manner into HZ*, LZa*, LZb*, LZc*, MZ*, UZa* and UZb* (Hoover, 1989a), as is the Upper Border Series (LZa', LZb', LZc', MZ', UZa', UZb' and UZc'; Salmonsen & Tegner, 2013). Again, primocryst compositions evolve continuously within this stratigraphic framework (e.g. Naslund, 1984; Hoover, 1989a; Salmonsen & Tegner, 2013). Primocrysts are generally slightly more primitive at the outer margins of the MBS than at the base of the LS (e.g. Fo_{74}, cpx-$Mg\#_{80}$), but are more Fe-rich in general (Hoover, 1989a). Bulk-rock incompatible element concentrations (e.g. P, Rb, U) suggest that the proportion of solidified trapped interstitial mush liquid was higher in the UBS (>30% in most zones; see below) and MBS (>30% in most zones) than in the corresponding sub-zones of the LS, especially after the appearance of cumulus Fe–Ti oxides (<10%; Wager & Brown, 1968; Hoover, 1989a; Tegner et al., 2009, 2011; Namur et al., 2013). This may be attributed to minimal compaction at the vertical walls and roof compared with the floor of the intrusion (Tegner et al., 2009, 2011).

SAMPLING AND ANALYTICAL METHODS

Samples
Samples used in this study include suites collected during three field seasons (2000, 2008 and 2011) and material from drill cores. The chosen suite of samples covers most of the stratigraphic units of the Layered Series (48 samples), the Marginal Border Series (15 samples) and the Upper Border Series (four samples; see Fig. 1 for locations and Supplementary Dataset 1 for details; supplementary data are available for downloading at http://www.petrology.oxfordjournals.org).

Analytical methods
Plagioclase compositions were obtained with a Cameca SX-100 electron microprobe (EPMA) at the University of Cambridge (Supplementary Datasets 2–4). Some data were acquired as single points, but most were acquired as single 30–1831 µm long traverses either from one crystal margin to another (rim–core–rim) or, more frequently, from core to rim along a straight line, with 4–80 single points, spaced at 5–61 µm, in each profile. This dataset totals more than 9640 microprobe analyses. Peak counting times were 20 s for major elements and 40 s for minor elements. Most data were acquired with a 15 kV and 10 nA beam with a spot size of 1 µm. Some profiles were also performed with a 25 kV and 100 nA beam to obtain accurate data for minor elements. Analyses that had a total outside the range 98·5–101 wt % were excluded. The following standards were used for Kα X-ray line calibration: diopside for Si and Ca; periclase for Mg; rutile for Ti; corundum for Al; fayalite for Fe; jadeite for Na; K-feldspar for K. Raw data were corrected with the CATZAF software.

SELECTING AND FITTING PLAGIOCLASE PROFILES
Three types of plagioclase core–rim compositional profiles have been reported from the Skaergaard intrusion (Maaloe, 1976; Toplis et al., 2008; Humphreys, 2009, 2011; Morse, 2012), as follows.

(1) Cores surrounded by a mantle of decreasing anorthite content [An, with $An = Ca/(Ca + Na)$ in molar fractions] followed by a rim of constant composition (Figs 2a, b and 3a). They are mostly found in meso- to orthocumulates of the Lower Zone of the Layered Series (Toplis et al., 2008). Some grains, however, show a slight decrease in An content in the external (outer) part of the rim (Toplis et al., 2008; Humphreys, 2009).

(2) Cores surrounded by rims of continuously decreasing An content (Figs 2c–e and 3a) in the Layered Series (Maaloe, 1976; Humphreys, 2009, 2011) and in the Marginal Border Series (Humphreys, 2011).

(3) Unzoned plagioclase grains (Figs 2f and 3a) in the Middle and Upper Zones of the Layered Series (Maaloe, 1976; Toplis et al., 2008).

Reverse zoning has also been reported in plagioclase from the Layered Series and has been attributed to crystallization in supercooled conditions (Maaloe, 1976), to a process of compaction-driven dissolution and reprecipitation (Humphreys, 2009) or to crystallization from an Fe-rich immiscible melt (Humphreys, 2011). It is worth noting that reverse zoning has not been observed in the plagioclase compositional profiles acquired in this study, which indicates that this type of zoning might be rather uncommon in the Skaergaard intrusion and potentially confined to the margins of pockets of Fe-rich liquid.
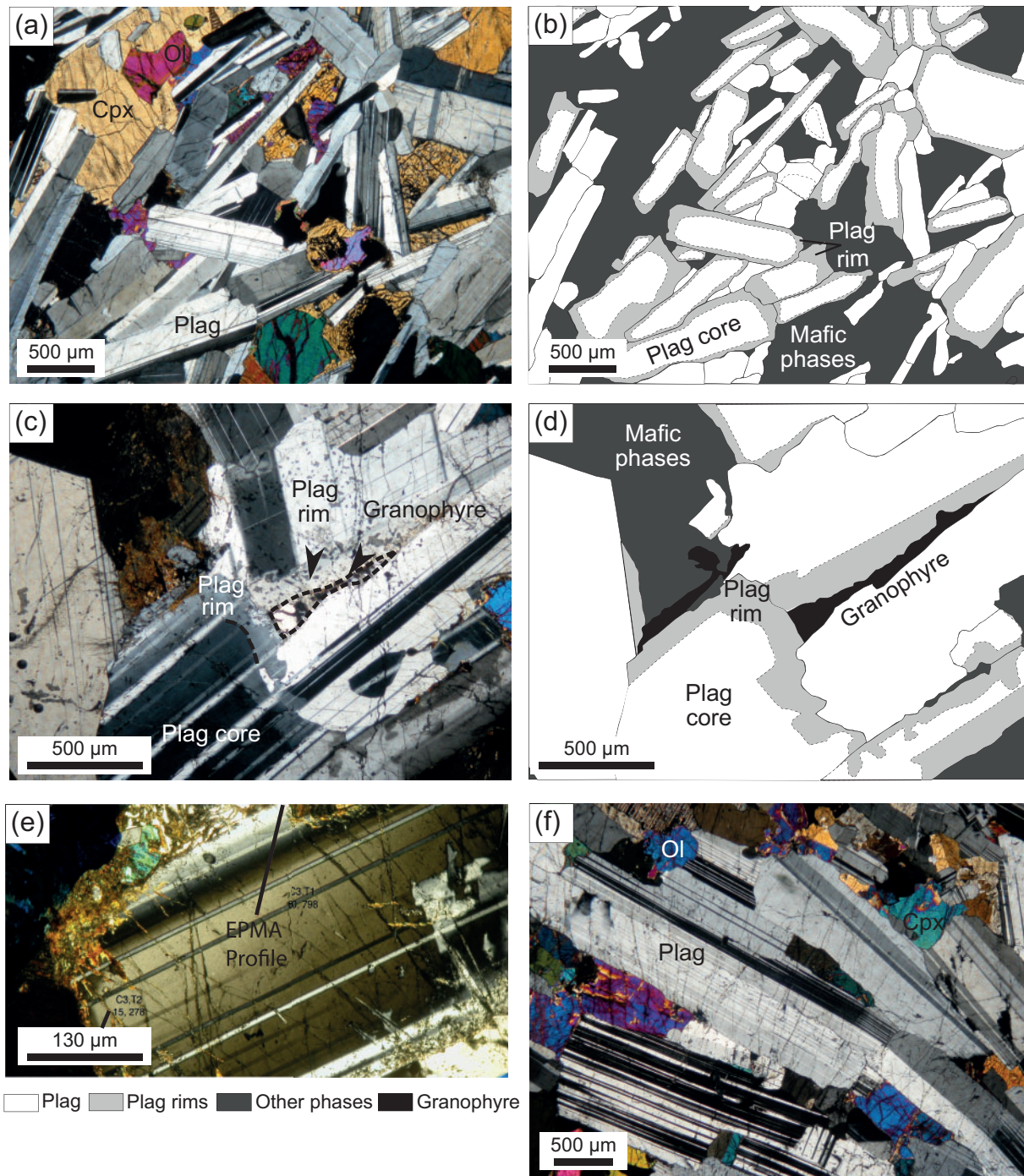
Fig. 2. Photomicrographs and line drawings illustrating the types of plagioclase grains observed in the Skaergaard intrusion. (a) Photomicrograph of sample 458252 (LZa). The presence of large plagioclase rims of uniform colour (buffered composition) should be noted. Cross-polarized transmitted light. (b) Line drawing of (a) showing the distribution of plagioclase buffered rims. Rims have been traced on high-resolution photographs with various orientations of the microscope stage. (c) Photomicrograph of sample 90-22-42l (UZb) showing the presence of a large granophyre pocket at the junction between plagioclase grains. The plagioclase rims (normal zoning down to An_{25}) at the contact with the granophyre pocket should be noted. Cross-polarized transmitted light. (d) Line drawing of (c) showing the distribution of plagioclase rims and granophyre pockets. (e) Normally zoned plagioclase grain in contact with a granophyre pocket. Profiles investigated by electron microprobe are shown for reference (EPMA profile). SKll-C2-4 (LZa*). Cross-polarized transmitted light. (f) Photomicrograph of sample SKGll-36 (LZc) showing unzoned plagioclase grains. The absence of evidence for evolved interstitial phases should be noted. Cross-polarized transmitted light.
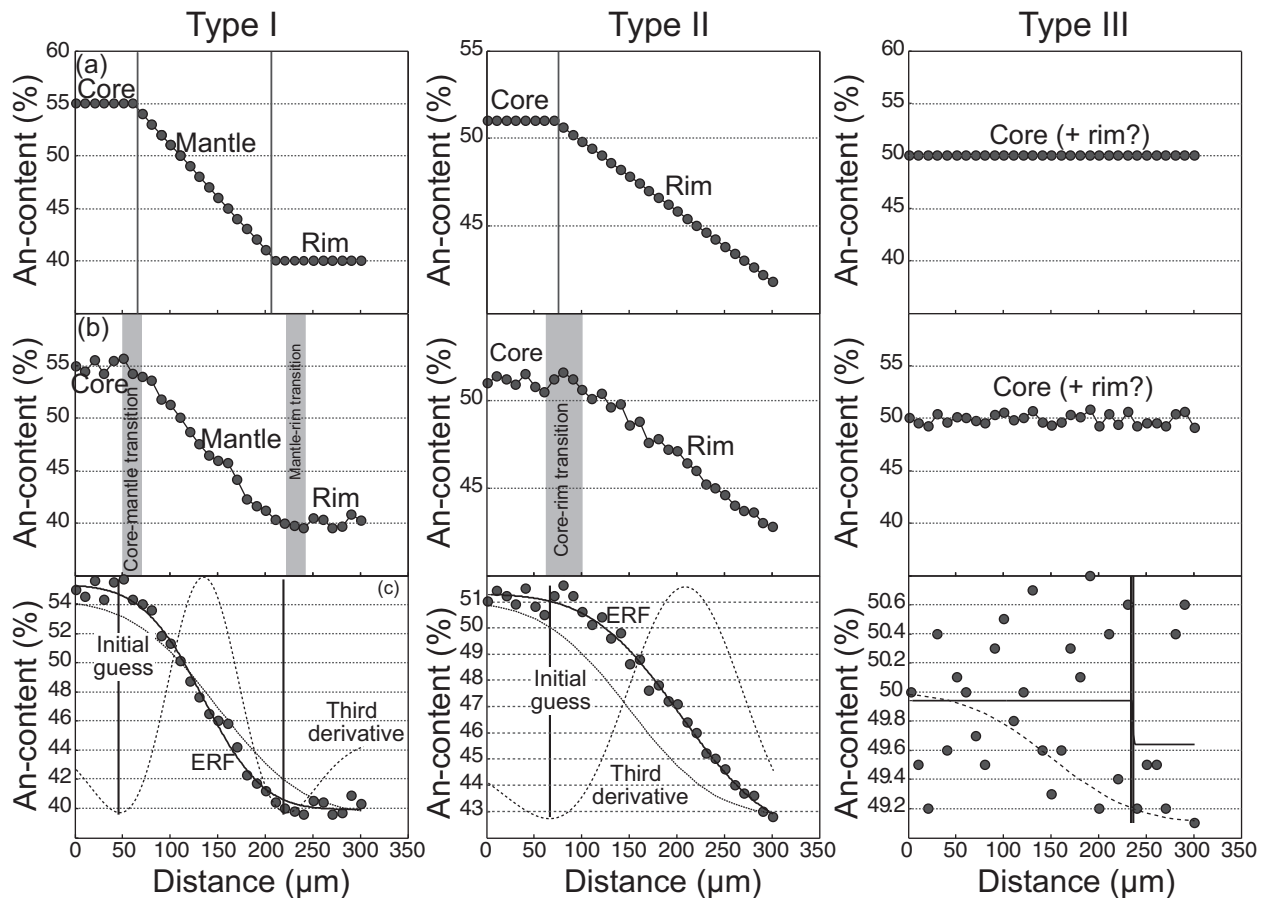
Fig. 3. (a) Theoretical types of plagioclase zoning (An vs distance) reported in the Skaergaard intrusion. Type 1: core of constant An content followed by a mantle of decreasing An content and a rim of constant An content; Type II: core of constant An content followed by a rim of decreasing An content; Type III: unzoned grain. (b) Illustration of similar plagioclase grains showing the natural variability of plagioclase composition in different zones and the effect of analytical uncertainty in electron microprobe measurements. It should be noted that determining the zones of the plagioclase profiles (core, mantle and rim) is somewhat ambiguous, as indicated by the grey vertical bars. (c) Best fit (continuous line) of an error function (ERF) on the plagioclase profiles. The dashed line represents the initial guess of the error function (see text for details). The vertical bars represent the boundaries between the zones of the plagioclase grains (core, mantle and rim) and are defined on the basis of the third derivative of the error function. The third derivative of the error function is shown for reference.

Most profiles were acquired from plagioclase grains in contact with another plagioclase grain because it has been suggested that the most evolved compositions may occur at plagioclase–plagioclase contacts (Toplis *et al.*, 2008). However, several profiles were also acquired from plagioclase grains in contact with other phases (olivine, clinopyroxene, magnetite, ilmenite). We did not observe any obvious compositional contrast in plagioclase rim compositions as a function of the adjacent phase. However, we note that Humphreys (2011) observed that the compositional profiles in plagioclase may change as a function of the modal mineralogy (e.g. proportion of Fe–Ti oxides vs pyroxenes) and texture (e.g. degree of igneous lamination) of the gabbros in the Skaergaard MZ.

We adopted a mathematical approach to describe and determine the relative size, which may be dependent on the cutting geometry, and composition of the different zones (Fig. 3b). We fitted an error function to each plagioclase profile (An vs distance), starting from a standard error function that could be elongated along the *y*-axis (An content) and the *x*-axis (distance), and rotated by 180°. This function, here called ERF_{An}, was calculated using the equation

$$ERF_{An} = a\ erf[b + (x/2)] + c \qquad (1)$$

where *a*, *b* and *c* are constant parameters to be regressed and *x* is the length (i.e. distance in μm) of the profile. The parameters *a*, *b* and *c* were regressed iteratively by minimizing the chi-squared (χ^2) value of the distribution with the maximum expected analytical error of the electron microprobe, here considered as being 1% An, and changing the parameters *a*, *b* and *c* to increase the quality of the fit. Simulations were stopped when (1) the lowest possible value of χ^2 was reached or (2) after 10 000 iterations.

To identify the zones (core, mantle, rim) of the An–distance profiles (Fig. 3c) we used the minimum values of the third derivative of ERF_{An} (d^3An/dx^3). This allows us to define the three types of profiles described above (Fig. 3, Table 1): (1) Type I profile [two minima in (d^3An/dx^3)] with a core of constant composition followed by a mantle of decreasing or increasing An content and a rim of constant composition; (2) Type II profile [one minimum in (d^3An/dx^3)] with a core of constant composition followed by a rim of decreasing or increasing An content; there is no mantle in this type of zoning profile; (3) Type III [no minima in (d^3An/dx^3)] profile with no zoning; there is neither a mantle nor rim in this type of zoning profile. Profiles were also considered as unzoned when the difference between the highest and lowest An values of ERF_{An} is lower than 2% An.

The global distribution of An content in each sample was assessed using two types of histogram using (1) the Kernel density distribution and (2) a Gaussian mixture model (Rudge, 2008; see Appendix for details on the calculation procedure). The two types of histograms were found to give similar results.

PLAGIOCLASE COMPOSITION
Layered Series

Plagioclase primocryst (core) compositions (Fig. 4a) in the LS evolve from *c.* $An_{70}Or_{1.0}$ at the base of LZa to *c.* $An_{35}Or_{3.5}$ at the top of UZb, in agreement with previous studies (Wager & Brown, 1968; McBirney, 1989; Humphreys, 2011).

Type I, Type II and Type III compositional profiles were identified in plagioclase crystals from the LS (Fig. 5; Table 1). Single grains are generally characterized by a single type of zoning profile (Type I, II or III), although Type I and Type II are locally observed on different faces of the same crystal. Most samples contain plagioclase crystals of different types (Type I, II and III; Fig. 5; Table 2), but a single type generally dominates within each sample. Quantifying the relative proportions of the three types is not straightforward and cannot be done accurately

without a detailed analysis or chemical mapping on the scale of an entire thin section. The results of an attempt to do this are shown in Fig. 5. We used high-resolution images of a subset of samples to produce a map of all plagioclase grains in each thin section. We then identified, using an optical microscope, the grains belonging to each type of profile (Type I, II and III) and used the software ImageJ to calculate the best-fit ellipses for each grain and estimate the relative proportion (vol. %) of each type of zoning profile. For all other samples, we report only the number of grains of each type analysed for this study (Table 2). Although we performed a detailed petrographic investigation of all the samples, the relative proportions of the three types of grains (Type I, II or III) that we measured may not be fully representative of their actual distribution in each sample.

Type I profiles (Tables 1 and 2) are very abundant from LZa to LZb, where they dominate the distribution of zoning types (See Figs 5 and 6 and the sketch in Fig. 2). Type I profiles are also common from MZ to the lower part of UZa (core $>An_{42}$), but they were not observed either in LZc or in samples from the upper part of UZa (core $<An_{42}$) to UZb (Fig. 6). Whereas the An content of the plagioclase cores decreases upwards in the stratigraphy, rim compositions fall into distinct and well-defined groups within the LS (Figs 7a–c, 8a–c and 9). In LZa samples, the rims have a constant composition of An_{54-58} (mode An_{56}; mean $An_{57.0}$; $n = 608$; where *n* is the number of analyzed points) regardless of the stratigraphic position of the sample (Fig. 9), whereas the rims have a constant composition of An_{49-53} (mode An_{50}; mean $An_{50.8}$; $n = 305$) in LZb and An_{40-43} (mode An_{41}; mean $An_{41.4}$; $n = 294$) from MZ to the lower part of UZa (core $>An_{42}$; Fig. 9). The global distribution of the An content in these samples (i.e. the distribution of all analysed compositions) is highly bimodal, with the first mode corresponding to the core composition and the second mode corresponding to the composition of the rim (Fig. 8a–c). In some grains, the outer part of the rim may, however, show a decrease in An content (see also fig. 5 in Humphreys, 2009). In some samples from LZa, Type I grains have two

Table 1: Types of plagioclase profiles observed in Skaergaard

Type of profile	Third derivative ERF function	Core	Mantle	Rim	Layered* Series	Marginal Border Border	Upper Border Series
Type I	2 minima	Constant An	Decreasing An	Constant An	LZa–LZb and MZ–UZa	LZa*–LZc*	LZa' and MZ'–UZa'
Type II	1 minima	Constant An	–	Decreasing An	LZa–LZb and MZ–UZb	LZa*–UZb*	LZb' and MZ'–UZa'
Type III	0 minima or △An <2	Constant An	–	–	LZc–UZb	LZa*	–

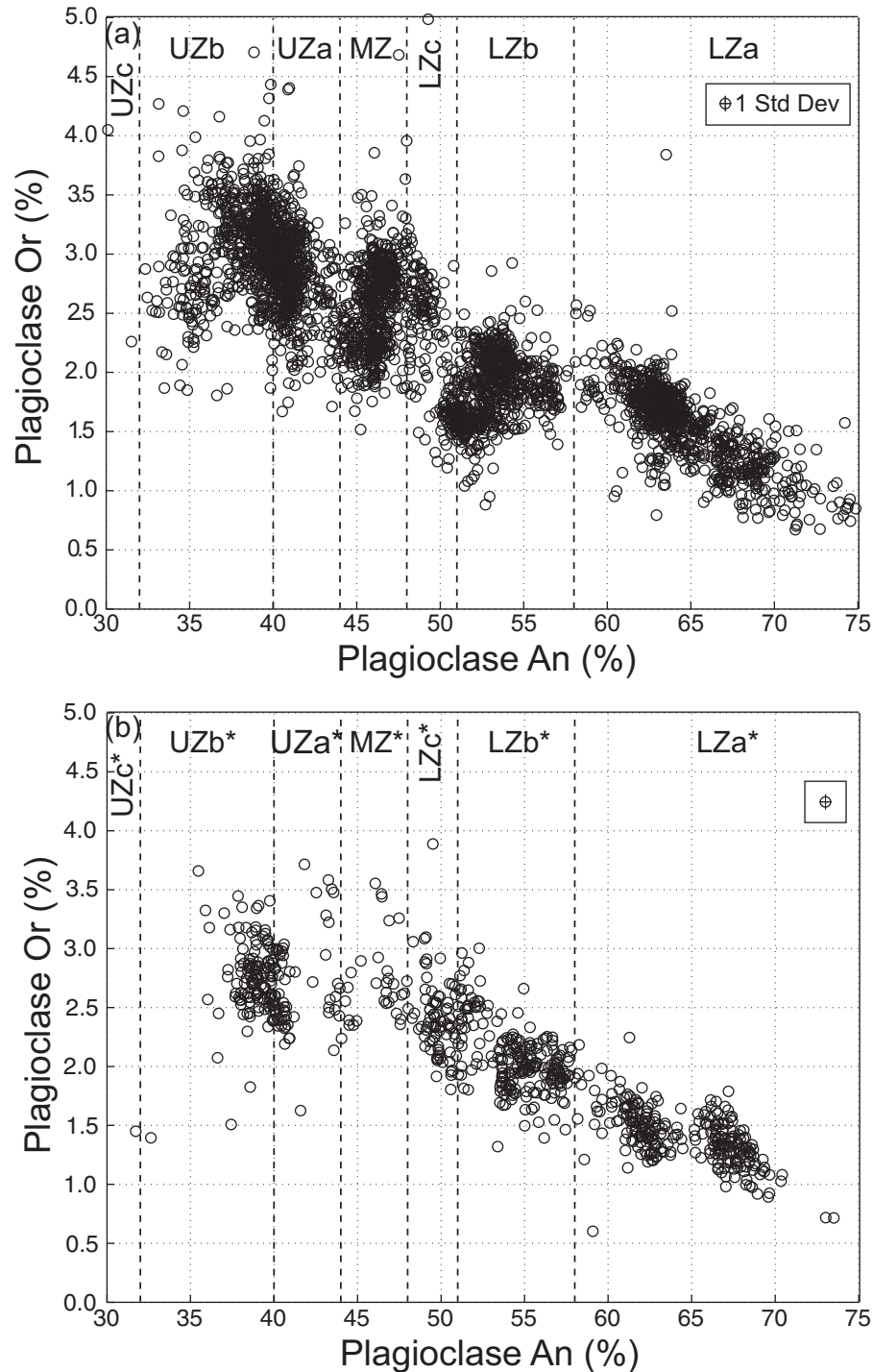*Units where the various types of zoning profiles are highly abundant.

Fig. 4. Orthoclase (Or) vs anorthite (An) content in plagioclase cores from (a) the Layered Series and (b) the Marginal Border Series.

clearly separate rims of constant composition. Such grains have a distinct core surrounded by an inner mantle of decreasing An content, an inner rim of An_{55-58}, a second mantle and then an outer rim of An_{50-51} (Fig. 10). It should also be noted that, in contrast to Ca and Na (i.e.

An content), the concentration of some minor elements, such as Ti and to a lesser extent Fe, continuously changes (generally decreases outwards or first increases and then decreases) within the rims of Type I grains (Humphreys, 2009, 2011).
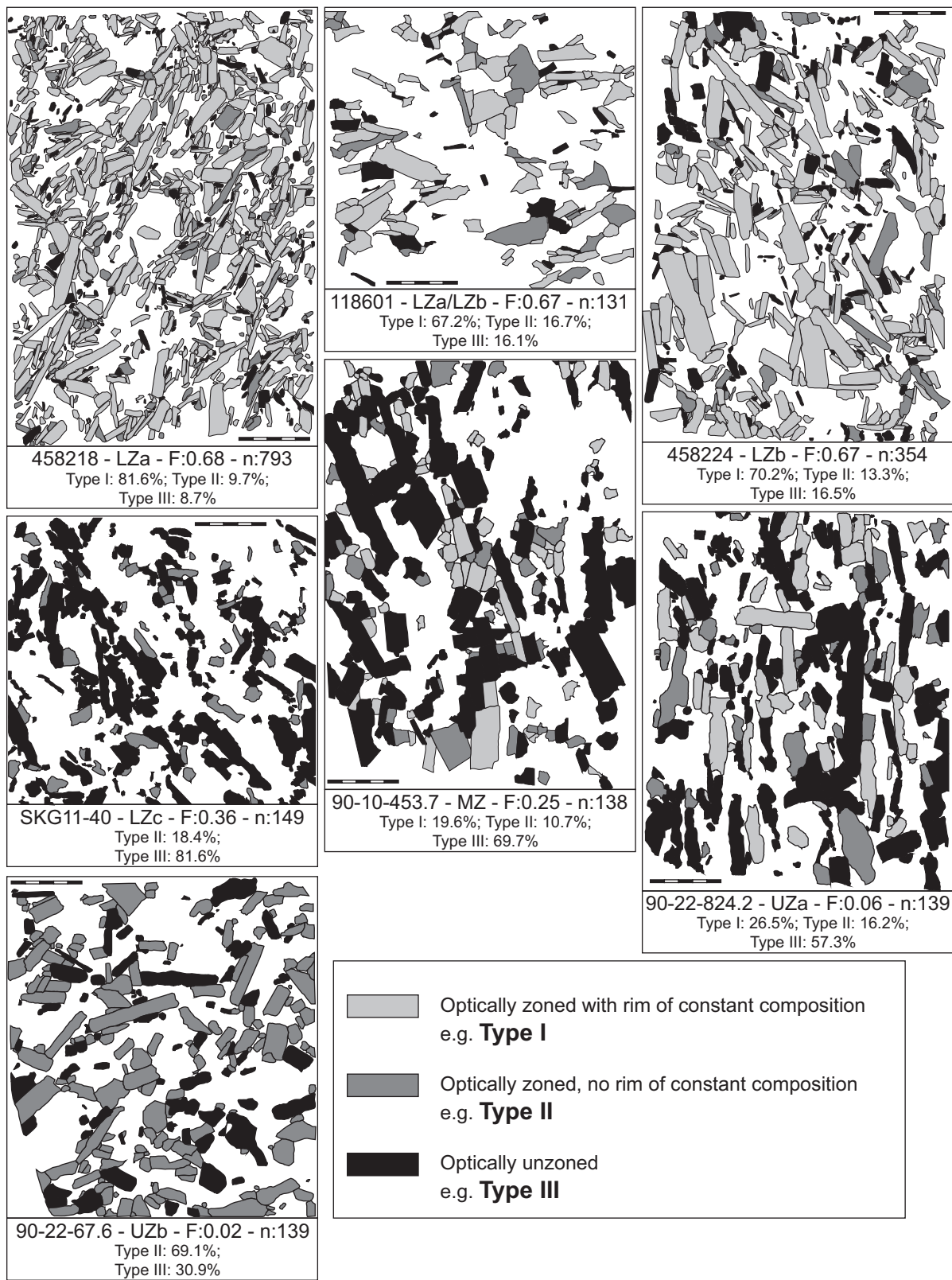
Fig. 5. Digitized texture maps of plagioclase crystals for selected samples of the Skaergaard Layered Series. Three types of plagioclase crystals with contrasted zoning types are shown; their relative proportions were determined using ImageJ software (see text for details). *n*, number of crystals; *F*, fraction of residual melt.

Table 2: Major element plagioclase zoning

Sample	F	Unit	P_2O_5 (wt %)[1]	Trapped liquid fraction[2]	Grains n	Single analyses n	Contact phases[3]	Type I grains n	Type II grains n	Type III grains n	Core 90[4] An%	Mantle Range An%	Rim Type I An%	Rim Type II An%	Core Or%	Mantle Or%	Rim Or%
Layered Series																	
Field samples																	
458242	0.75	LZa	0·14	0·38	8	305	Plag, cpx, ox	8	-	-	68-69	69-56	56-58	-	0·8-1·3	1·1-1·7	1·4-2·0
458214	0.71	LZa	0·14	0·41	6	214	Plag, ol	5	1	-	64-65	65-55	55-58	65-57	1·1-2·0	1·5-1·7	1·7-2·8
458218	0.68	LZa	0·14	0·41	4	93	Plag, cpx	4	-	-	62-63	63-55	55-56	-	1·6-2·0	1·7-2·1	2·1-3·0
458224	0.67	LZb	0·11	0·31	6	184	Plag, ol, cpx	5	1	-	61-62	62-49	49-52	62-49	1·6-2·2	1·8-2·8	2·0-2·8
458231	0.57	LZb	0·10	0·24	1	35	Plag	1	-	-	55-56	56-50	50-51	-	2·2-2·6	2·4-2·7	2·7-3·0
458205	0.46	LZb	0·10	0·21	6	135	Plag, cpx, gr	4	2	-	56-57	57-49	49-50	57-48	1·7-2·1	2·0-2·3	2·3-2·8
SKG11-23	0.40	LZb	-	-	5	179	Plag, cpx	1	4	-	54-55	55-50	49-50	55-50	1·5-2·2	-	1·8-2·4
SKG11-27	0.39	LZb	-	-	8	218	Plag, cpx, ox	7	1	-	53-56	56-50	50-51	56-50	1·7-2·1	1·9-2·3	2·1-2·6
SKG11-28	0.38	LZb	-	-	3	78	Cpx	3	-	-	54-55	55-50	50-51	-	2·1-2·3	2·1-2·4	2·1-2·6
SKG11-29	0.38	LZb	-	-	8	124	Plag, cpx	4	2	2	53-55	55-49	49-51	55-51	1·6-2·2	1·7-2·1	2·0-2·3
458279	0.38	LZb-LZc	0·06	0·11	2	27	Plag	1	1	-	52-53	53-49	49-50	53-50	1·8-2·0	1·8-2·2	2·2-2·4
SKG11-36	0.37	LZc	-	-	5	206	Plag, cpx, ox	-	-	5	49-51	-	-	-	1·6-2·9	-	-
SKG11-40	0.36	LZc	-	-	3	40	Plag, cpx, ox	-	-	3	50-52	-	-	-	1·6-1·8	-	-
SKG11-43	0.35	LZc	-	-	5	77	Plag, cpx, ox	-	-	5	51-52	-	-	-	1·6-2·2	-	-
458286	0.35	LZc	0·02	0·04	3	166	Plag, cpx	-	-	3	50-52	-	-	-	1·1-2·1	-	-
458287	0.33	LZc	0·02	0·04	2	176	Plag, cpx	-	-	3	50-52	-	-	-	1·5-1·8	-	-
1966 drill core																	
1045'	0.84	LZa	-	-	3	118	Plag, ol, cpx	2	1	-	68-70	70-57	57-58	70-57	1·1-1·5	1·2-1·9	1·5-2·3
9371'1''	0.82	LZa	-	-	4	101	Plag, cpx	2	2	-	68-72	72-56	56-58	72-58	0·8-1·5	1·1-1·8	1·5-2·2
118678	0.78	LZa	-	-	12	405	Plag, ol, cpx, ox	8	3	1	63-65	65-55	55-57	65-55	1·2-1·9	1·6-2·1	1·5-2·5
6617''	0.77	LZa	-	-	3	117	Plag	3	-	-	65-67	67-55	56-58	-	1·1-1·7	1·3-1·7	1·3-1·9
118653	0.74	LZa	-	-	5	192	Plag, ol	4	1	-	63-65	65-55	55	65-55	1·4-1·7	1·6-2·3	1·9-2·7
316'	0.71	LZa	-	-	5	121	Plag, cpx, ox	4	1	-	62-64	64-54	54-55	64-54	1·3-1·9	1·7-2·3	1·5-2·3
3196'5''	0.71	LZa	-	-	3	121	Plag, ol	3	-	-	62-63	63-54	54-55	-	1·5-2·1	1·7-2·0	1·7-2·7
118601	0.67	LZa-LZb	-	-	2	69	Plag, ol	-	2	-	59-62	-	54-55	-	1·5-1·9	-	1·8-2·4
118605	0.67	LZa-LZb	-	-	3	79	Plag, ol	1	1	1	59-61	61-55	55-58	61-55	1·5-1·8	-	1·4-2·4

(continued)

Table 2: Continued

Sample	F	Unit	P_2O_5 (wt %)[1]	Trapped liquid fraction[2]	Grains n	Single analyses n	Contact phases[3]	Type I grains n	Type II grains n	Type III grains n	Core 90[4] An%	Mantle Range An%	Rim Type I An%	Rim Type II An%	Core Or%	Mantle Or%	Rim Or%
Platinova 90-10 core																	
90-10-456	0·25	MZ	–	–	4	41	Plag, ox	–	1	3	48–50	–	–	50–46	2·1–2·8	–	–
90-10-453.7	0·25	MZ	–	–	9	167	Plag, cpx	7	2	–	47–49	49–41	41–42	49–41	1·7–2·9	2·0–3·4	1·6–3·7
90-10-444.8	0·24	MZ	–	–	4	138	Plag, cpx, ox	1	–	3	47–49	49–42	42–41	–	2·3–2·8	2·5–2·9	2·8–3·1
90-10-444.35	0·24	MZ	–	–	2	73	Plag, cpx	2	–	–	48–49	49–40	40–41	–	2·3–2·9	2·5–2·9	2·8–3·1
90-10-440.5	0·23	MZ	–	–	3	57	Plag, cpx	2	1	–	46–48	48–40	40–41	48–40	2·7–3·4	2·8–4·1	2·7–4·6
90-10-431.45	0·22	MZ	–	–	2	109	Plag, cpx	1	1	–	45–47	47–40	40–42	47–40	2·5–3·2	2·8–3·2	3·1–3·9
90-10-212	0·14	UZa	–	–	6	131	Plag, cpx, ox	4	1	1	45–46	46–39	39–40	46–40	2·0–2·9	2·3–3·0	2·1–3·1
90-10-210.15	0·14	UZa	–	–	3	74	Cpx	2	–	1	45–46	46–39	39–41	–	2·1–2·8	2·5–3·0	2·4–3·5
90-10-524	0·32	MZ	–	–	2	31	Plag	1	1	–	47–48	48–40	40–41	48–40	1·9–2·3	2·2–2·6	2·1–2·8
Platinova 90-22 core																	
90-22-824.2	0·19	UZa	0·06	0·06	14	330	Plag, cpx, ox	8	–	6	46–47	47–40	40–41	–	1·9–2·6	2·3–2·6	2·1–2·9
90-22-689	0·15	UZa	0·05	0·04	5	103	Cpx, ol, ox	4	–	1	43–45	45–40	40–41	–	1·7–2·4	2·0–2·4	2·4–3·1
90-22-585.8	0·13	UZa	0·08	0·04	6	124	Plag, cpx	–	6	–	40–42	–	–	42–28	2·3–3·4	–	3·0–4·1
90-22-491.84	0·10	UZa	0·08	0·04	8	143	Plag, cpx	–	2	6	39–42	–	–	42–26	2·5–3·0	–	–
90-22-481.8	0·10	UZa	0·07	0·04	13	301	Plag, cpx, gr, ox	1	12	–	39–42	42–35	35–33	42–17	2·6–3·3	2·6–4·1	2·3–4·6
90-22-481.2	0·10	UZa	0·07	0·04	8	132	Plag, cpx, gr	–	5	3	40–41	–	–	41–22	2·5–3·2	–	2·6–4·1
90-22-480	0·10	UZa	0·07	0·04	10	157	Plag, cpx, gr	–	7	3	40–42	–	–	42–24	2·1–3·5	–	2·9–4·6
90-22-479.2	0·10	UZb	–	–	7	155	Plag, gr, cpx	–	5	2	39–42	–	–	42–25	2·3–3·6	–	2·8–5·4
90-22-461.8	0·09	UZb	–	–	12	266	Plag, cpx, ox	–	5	7	40–42	–	–	42–33	2·5–3·4	–	–
90-22-421	0·09	UZb	–	–	10	233	Plag, gr, ol, cpx	–	10	–	38–40	–	–	40–25	2·3–4·1	–	2·9–6·5
90-22-323.8	0·06	UZb	–	–	5	68	Plag, gr, ol	–	4	1	37–39	–	–	39–30	3·1–3·7	–	3·1–4·4
90-22-210.9	0·04	UZb	–	–	7	133	Plag, ol	–	5	2	36–39	–	–	39–24	2·7–4·1	–	2·4–4·6
90-22-107.7	0·03	UZb	–	–	4	73	Plag, gr, cpx	–	4	–	34–35	–	–	35–10	2·4–3·3	–	2·1–4·2
90-22-67.6	0·02	UZb	–	–	8	117	Plag, cpx, ol	–	8	–	35–37	–	–	37–7	1·8–2·9	–	3·0–6·7

(continued)

Table 2. Continued

Sample	F	Unit	P₂O₅ (wt %)[1]	Trapped liquid fraction[2]	Grains n	Single analyses n	Contact phases[3]	Type I grains n	Type II grains n	Type III grains n	Core 90[4] An%	Mantle Range An%	Rim Type I An%	Rim Type II An%	Core Or%	Mantle Or%	Rim Or%
Marginal Border Series																	
Field samples																	
KR-02-4	0.84	LZa*	–	–	4	49	Plag, cpx	–	4	–	69-73	–	–	73-60	0.6-0.8	–	0.7-1.4
KR-02-37	0.81	LZa*	0.12	0.41	8	150	Plag, cpx	5	3	–	66-69	69-55	55-58	69-55	1.3-1.7	1.4-1.9	1.6-2.6
SP60	0.71	LZa*	0.12	0.35	9	255	Plag	7	2	–	65-68	68-55	55-58	68-36	1.0-1.6	1.3-1.8	1.6-2.4
SP46	0.68	LZa*–LZb*	0.11	0.33	11	310	Plag, cpx	7	4	–	59-62	62-49	49-51	62-30	1.3-1.8	1.4-2.2	2.0-3.1
KR-02-21	0.60	LZb*	0.14	0.45	4	39	Plag	–	4	–	59-60	–	–	60-30	1.5-2.0	–	1.9-3.5
SK11-C14-C3	0.57	LZb*	0.12	0.35	7	190	Plag, gr	–	7	–	54-57	–	–	57-0	2.1-3.0	–	0.5-7.2
SP8	0.55	LZb*	0.13	0.48	6	55	Plag, cpx, ol	–	6	–	55-57	–	–	57-43	1.5-2.0	–	1.7-3.2
SK11-C1-6	0.45	LZb*	0.17	0.41	8	208	Plag, cpx	–	8	–	57-58	–	–	58-16	1.3-2.6	–	2.4-6.7
SK11-C2-4	0.39	LZb*	0.12	0.34	8	242	Plag, gr, cpx	–	8	–	50-54	–	–	54-16	1.8-2.7	–	2.0-7.0
SP16	0.35	LZc*	0.09	0.28	9	145	Plag, cpx	2	7	–	51-52	52-41	41-40	52-37	2.4-2.8	1.3-2.1	2.6-4.4
SP20	0.25	MZ*	–	–	10	171	Plag, cpx, ox	–	8	2	49-51	–	–	51-18	1.8-2.5	–	2.0-4.9
SP26	0.15	UZa*	–	–	4	89	Plag, gr	–	4	–	42-45	–	–	45-18	2.0-3.1	–	2.5-7.0
SP29	0.06	UZb*	–	–	2	17	Plag	–	2	–	37-38	–	–	38-18	2.7-3.0	–	2.9-4.2
SK11-C11-3	0.05	UZb*	–	–	4	147	Plag, gr	–	4	–	39-40	–	–	40-16	2.3-2.9	–	0.6-5.5
SK11-C12-1	0.03	UZb*	–	–	6	179	Plag, cpx, gr	–	6	–	38-40	–	–	40-3	1.9-3.6	–	0.3-8.2
Upper Border Series																	
Field samples																	
SK08-159	0.68	MZ'	0.27	0.33	5	162	Plag, cpx, gr	2	3	–	45-47	47-40	40-39	29-3	2.8-3.6	2.8-7.2	0.5-7.8
SK08-140	0.55	Uza'	0.29	0.31	5	187	Plag, ol, gr	1	4	–	45-47	47-41	41-40	20-37	2.7-3.8	2.5-3.1	3-11.2
SK08-119	0.21	LZa'	0.08	0.21	5	101	Plag, cpx, ol	5	–	–	65-67	67-55	55-57	–	1.1-1.9	1.5-2.2	1.6-2.8
SK08-124	0.17	LZb'	0.18	0.43	5	203	Plag, cpx	–	5	–	56-58	–	–	24-43	1.6-2.2	–	2.1-4.9

[1] Data from Tegner et al. (2009), Namur et al. (2013), Salmonsen & Tegner (2013) and unpublished data.
[2] Calculated from the P₂O₅ bulk-rock content (see Appendix for details).
[3] Plag, plagioclase; ol, olivine; cpx, clinopyroxene; ox, Fe–Ti oxides; gr, granophyre.
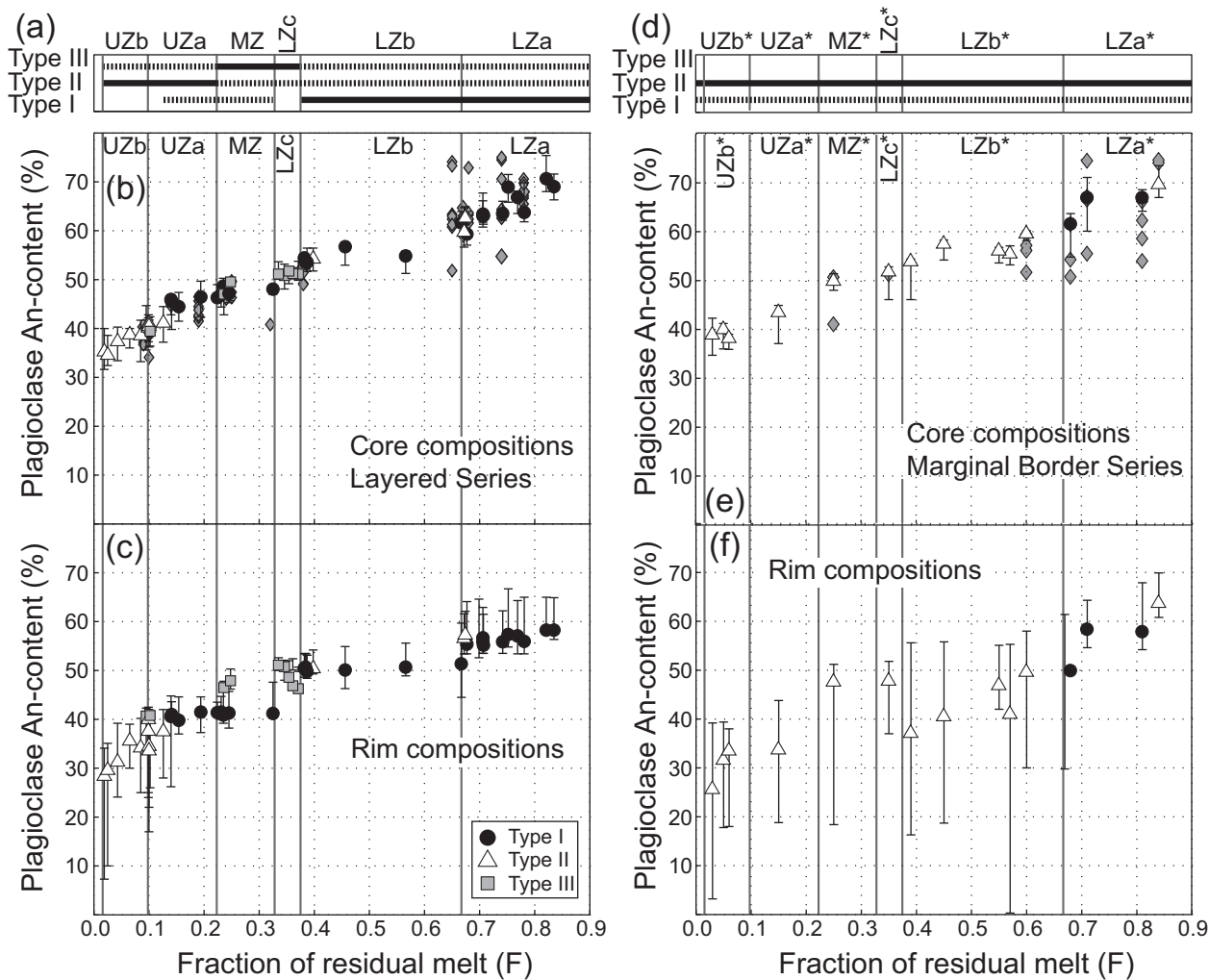[4] Compositional range for 90% of the measurements centred on the mean.

Fig. 6. Plagioclase compositional variations in the Skaergaard Layered Series and Marginal Border Series. (a) Stratigraphic distribution of the types of zoning profile (Type I, II and III) in the Layered Series. Continuous lines, highly abundant; dashed lines, locally present. (b) Mode (symbol) and range of core compositions in single samples from the Layered Series. (See text for details on the procedure to discriminate between core, mantle and rim.) Data are symbol- and shading-coded as a function of the dominant type of zoning profile (Type I, II and III) in each sample. (c) Mode and range of rim (or mantle + rim) compositions in the Layered Series. (d) Stratigraphic distribution of the types of zoning profiles (Type I, II and III) in the Marginal Border Series. (e) Mode (symbol) and range of core compositions in single samples from the Marginal Border Series. (f) Mode and range of rim (or mantle + rim) compositions in the Marginal Border Series. Diamonds are single microprobe analyses from Humphreys (2011).

The orthoclase content in compositional profiles from Type I plagioclase grains evolves in the opposite way to the An content (Fig. 11a), but the width of the rim with constant Or content may locally be different from that of the An rim. This difference may result from faster subsolidus diffusion of K:Na compared with Ca:Na, especially in plagioclase with low An content (Giletti & Shanahan, 1997).

Type II plagioclase grains (Fig. 7d and e) are observed from LZa to LZb and from MZ to UZb (Fig. 6; Table 2). The most evolved composition of the rims (i.e. the average of the outermost three measurements) changes significantly from one zone to another in the LS. It is generally

in the range $An_{55–58}$ (mean $An_{56\cdot4}$; $n = 11$; Table 2; Fig. 6) in LZa, from An_{48} to An_{51} (mean $An_{50\cdot3}$; $n = 9$; Fig. 5e) in LZb and from An_{40} to An_{41} (mean $An_{40\cdot8}$; $n = 7$) from MZ to the lower part of UZa (core $>An_{42}$). It is worth noting that these compositions are identical to the compositions of the rims observed in Type I grains (Fig. 6). From the top of UZa (core $<An_{42}$) to UZb, the most external values from the various profiles span a very large range from An_{42} to An_5 (mean $An_{29\cdot2}$; $n = 63$; Fig. 6; Table 2). The global distribution of the plagioclase An content in single samples is unimodal (generally with a long negative tail), or slightly bimodal when Type II and Type I grains coexist in the same sample (Fig. 8d and e). The orthoclase
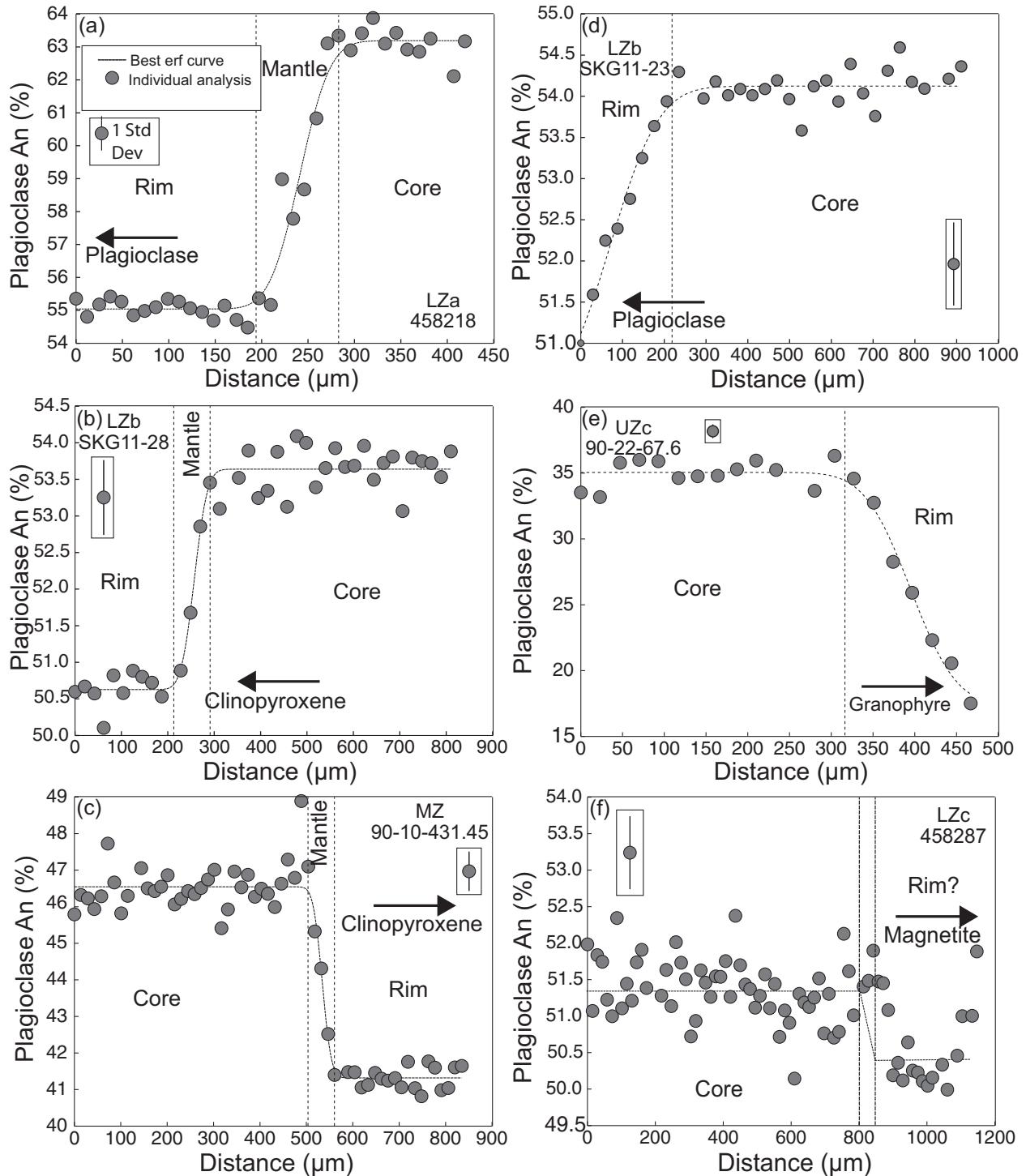
Fig. 7. Examples of plagioclase profiles in the Layered Series. (a) Type I profile, 458218, LZa. It should be noted that the rim is buffered to a constant composition of An_{55}. (b) Type I profile, SK11-28, LZb. The rim is buffered to a constant composition of An_{51}. (c) Type I profile, 90-10-431.45, MZ. The rim is buffered to a constant composition of An_{41}. (d) Type II profile, SKG11-23, LZb. It should be noted that the most evolved composition of the rim is An_{51}. (e) Type II profile, 90-22-67.6, UZc. (f) Type III profile, 458287, LZc.
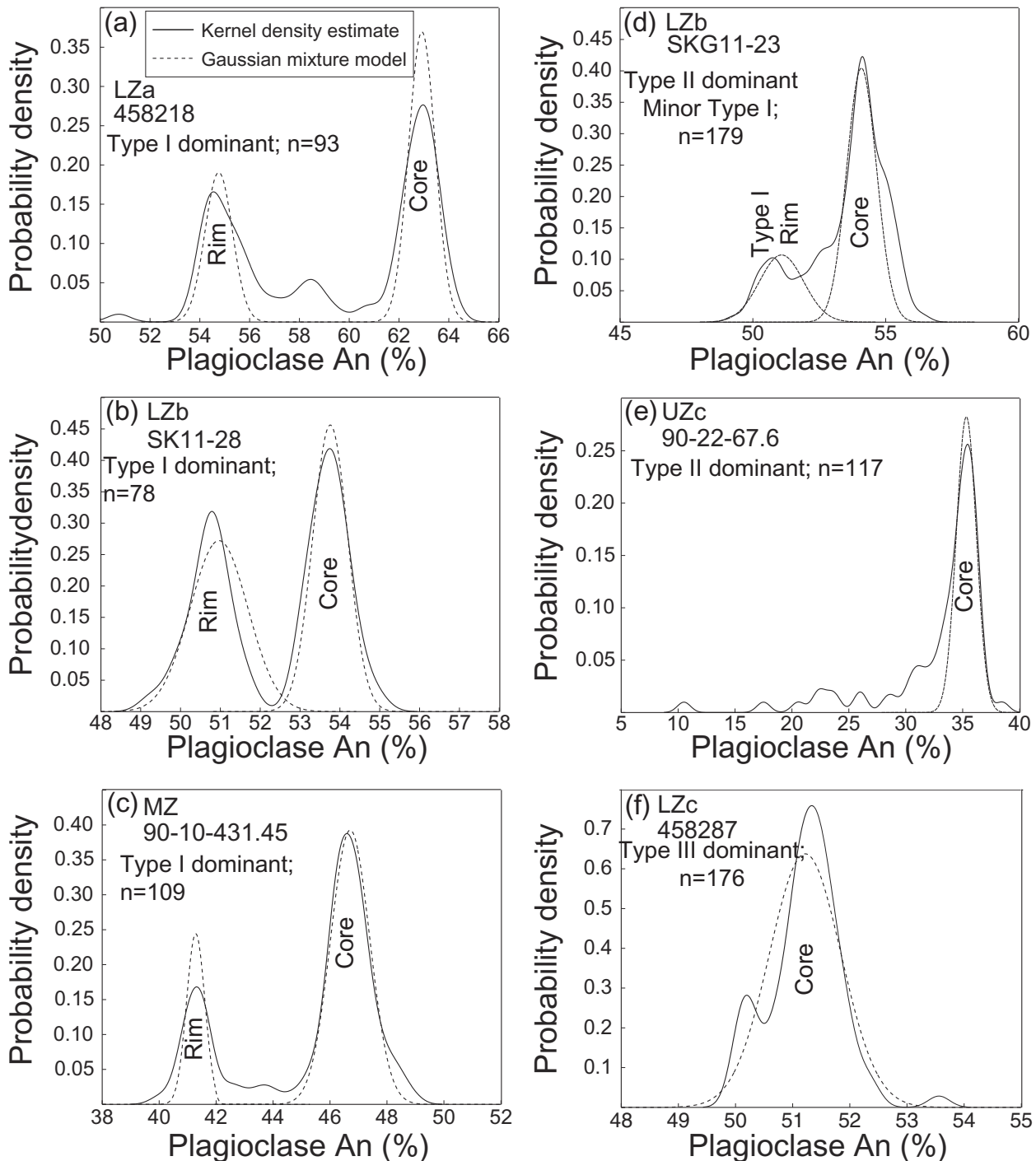
Fig. 8. Global distribution (density probability function) of An content in selected samples from the Layered Series (see representative compositional profiles for the same sample in Fig. 7). For simplicity, the density function can be understood as the relative proportion of each composition (0–1) calculated from the number of observations (*n*). Reported data include compositions from the cores, the mantles (if present) and the rims. The global distribution has been calculated in two ways: a Kernel density distribution and a mixture of Gaussian curves (see Appendix for details on the calculation procedure). These two ways to represent the global distributions are more statistically robust than simple histograms for which the size of the bins has to be selected arbitrarily. (a–c) Samples dominated by grains with Type I compositional profiles. The well-defined bimodal distribution, with the first mode corresponding to the core compositions and the second mode corresponding to the rim compositions, should be noted. (d, e) Samples dominated by Type II compositional profiles. It should be noted that the global distribution of An is unimodal (possibly with a long negative tail) or slightly bimodal (when Type I and Type II profiles coexist in a given sample). (f) Sample dominated by Type III compositional profiles. The unimodal distribution of An should be noted.
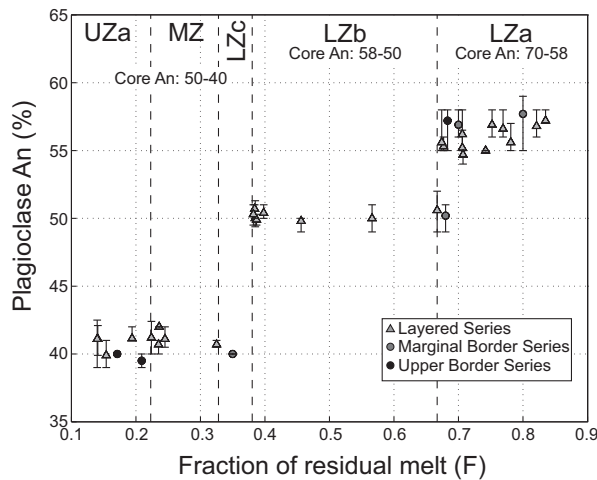
Fig. 9. Composition of rims of Type I grains as a function of stratigraphic position (fraction of remaining liquid; Nielsen, 2004). Error bars correspond to the compositional range of rims observed in single samples. Ranges of core compositions are shown for reference.

content in Type II plagioclase grains evolves in the opposite direction to the An content (Fig. 11b), but starts to decrease when the plagioclase An content becomes lower than 22–25.

Unzoned (ΔAn lower than 2%) Type III plagioclase grains are mostly found from LZc to UZb (Table 1; Figs 6 and 7f). They show a unimodal distribution of plagioclase An contents and minor variation in Or content (Fig. 8f).

Marginal Border Series

Plagioclase core compositions in the MBS evolve continuously from c. An_{70} and Or_1 in LZa* to c. An_{35} and Or_3 in UZb*, in a similar way to plagioclase in the LS (Fig. 4b).

The MBS is dominated by Type II plagioclase grains (Tables 1 and 2; Fig. 6). In these samples, the core composition continuously evolves as a function of the stratigraphic position (Fig. 6), whereas the rims of single grains show normal zoning (e.g. decreasing An content; Fig. 12a). The outermost edge of the rims spans a very large range of compositions: An_{29-69} (mean An_{50}; $n = 17$) in LZa* (Fig. 6), An_{3-60} (mean An_{36}; $n = 42$) in LZb*, An_{18-46} (mean An_{37}; $n = 21$) in the interval between LZc* and the lower part of UZa*, and An_{2-40} (mean An_{23}; $n = 12$) in the upper part of UZa* and UZb*. The global distribution of An content in these samples is generally unimodal (Fig. 12b).

Type I plagioclase grains have been observed in three samples from the external part of the MBS (two samples in LZa* and one sample in LZb*; Tables 1 and 2). Similar to Type I plagioclase in the LS, they have a rim with a constant composition of An_{55-58} (mean $An_{57.5}$; mode An_{57}; $n = 100$; Figs 9 and 12c, d) in LZa* and An_{49-52} (mean $An_{50.2}$; mode An_{50}; $n = 42$) in LZb* (Figs 6 and 12e, f).
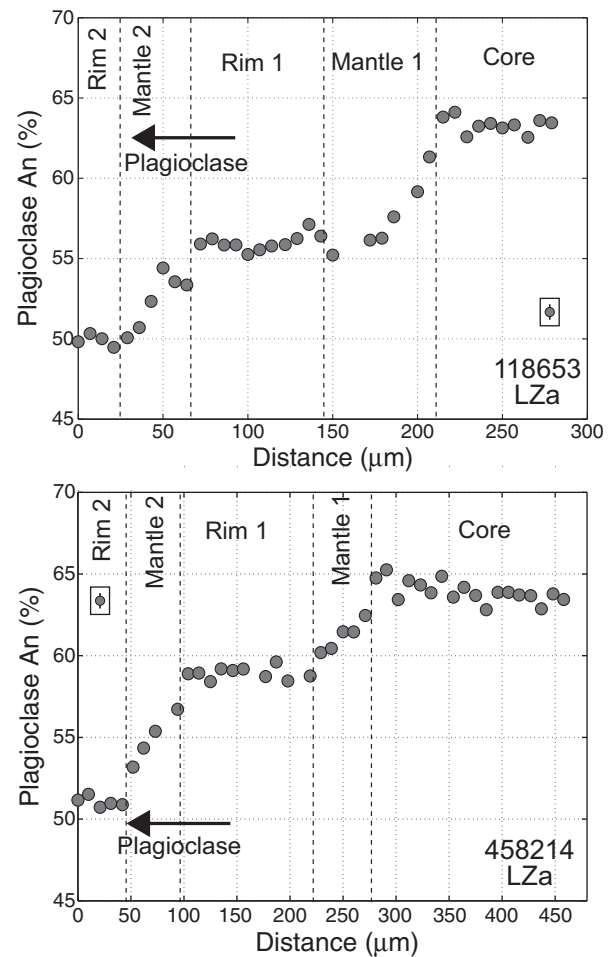

Fig. 10. Examples of Type I plagioclase grains in LZa showing a core surrounded by two different mantles of decreasing An content and two rims buffered to a constant composition (rim 1: An_{55-58}; rim 2: An_{50-51}).

These values are identical to those of rims of the Type I grains in the LS (LZa and LZb).

Type III (unzoned) plagioclase grains are a very minor feature in the MBS and we measured only a single unzoned grain in SP-20 (MZ*; An_{43-45}; $Or_{2.8-3.1}$).

Upper Border Series

Plagioclase core compositions in the UBS evolve continuously from c. An_{67} and Or_1 in LZa' to c. An_{45} and Or_3 in UZa' (Table 2). The UBS is dominated by Type I and Type II plagioclase grains (Tables 1 and 2). We did not observe any Type III plagioclase grains.

Type I plagioclase grains were observed in LZa', MZ' and in the lower part of UZa' (core >An_{42}). The rim has composition An_{55-57} (mean $An_{56.5}$; mode An_{56}; $n = 23$) in LZa' and An_{39-41} (mean $An_{40.3}$; mode An_{40}; $n = 43$) in MZ' and UZa', identical to the values observed in the LS and MBS (Fig. 9).
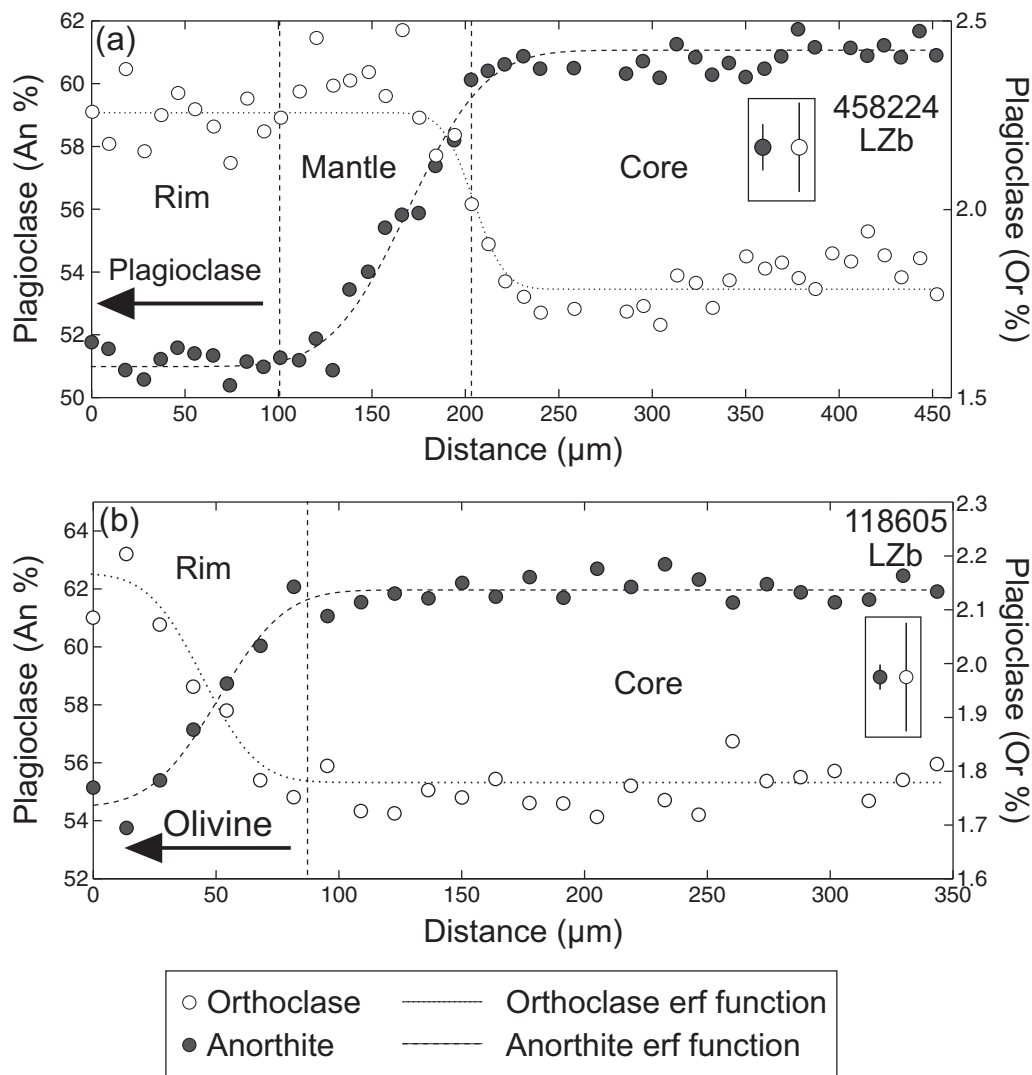
Fig. 11. Comparison of An content vs distance and Or vs distance compositional profiles in plagioclase grains. (a) Type I profile, 458224, LZb. (b) Type II profile, 118605, LZb. Different error functions have been fitted to the An profile and the Or profile. The boundaries between the zones (core, mantle and rims) are based on the An error function.

Type II plagioclase grains were observed in LZb', MZ' and UZa'. The outermost edge of the rims spans a large range of compositions from An_{24} to An_{43} (mean An_{34}; $n = 5$) in LZb' and An_3 to An_{38} (mean An_{28}; $n = 8$) in the interval between MZ' and the lower part of UZa'.

Summary of the key compositional observations in plagioclase profiles

Three main types of plagioclase compositional profiles are observed in the Skaergaard intrusion. Type I grains show a core of constant composition, surrounded by a mantle of decreasing An content and a rim of constant composition. They are abundant in the Layered Series LZa and LZb, and are also common in MZ and UZa. They are absent from LZc and UZb. The core composition evolves continuously as a function of the stratigraphic position but the rims show only three compositions: $An_{56\pm2}$ in LZa (and equivalent units in the MBS and UBS), $An_{51\pm1}$ in LZb and $An_{41\pm1}$ in MZ–UZa (Fig. 13). Type II grains also have a core of constant composition surrounded by a rim of decreasing An content. In most of the LS (LZa–LZb), the rims show relatively restricted ranges of compositions and generally do not evolve to An contents lower than those observed in the rims of Type I grains (Fig. 13). In contrast, in UZa as well as in the MBS and UBS, Type II grains are very abundant and the rims locally show very evolved compositions down to An_{5-10} (Fig. 13). Type III grains are mostly observed in the LS from LZc to UZb and are unzoned.
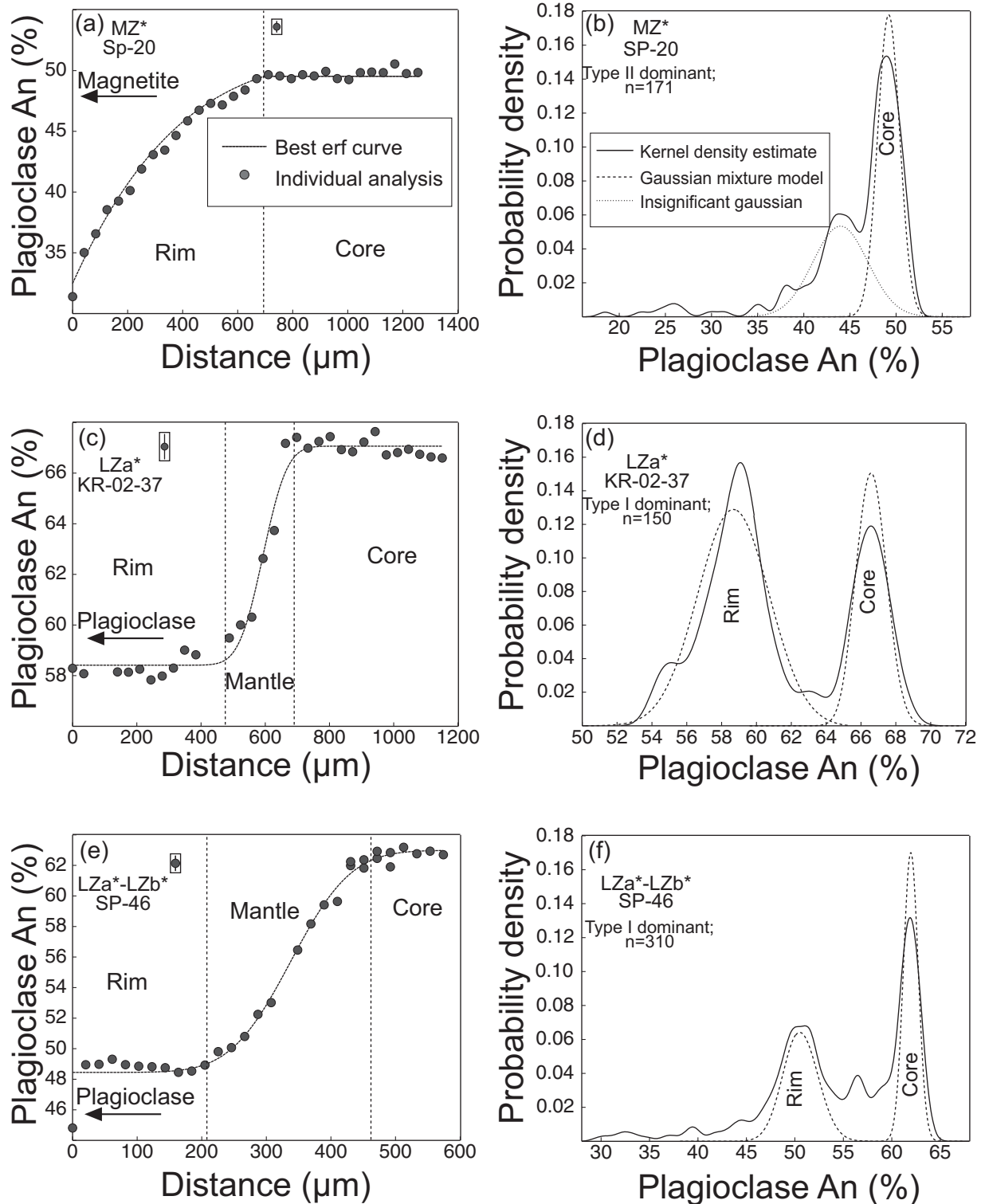
Fig. 12. Examples of plagioclase profiles (An vs distance) in the Marginal Border Series. (a) SP-20, MZ*, Type II. (c) KR-02-37, LZa*, Type I. It should be noted that the rim is buffered to a composition of An_{58}. (e) SP-46, LZa*–LZb*, Type I. The rim is buffered to a composition of An_{49}. (b, d, f) Histograms showing the global distribution (density probability function) of An content in the same three samples (SP-20; KR-02-37; SP-46). The significance of the Gaussian curves (e.g. Insignificant Gaussian) was determined with SiZer plots (Rudge, 2008; see Appendix for details).
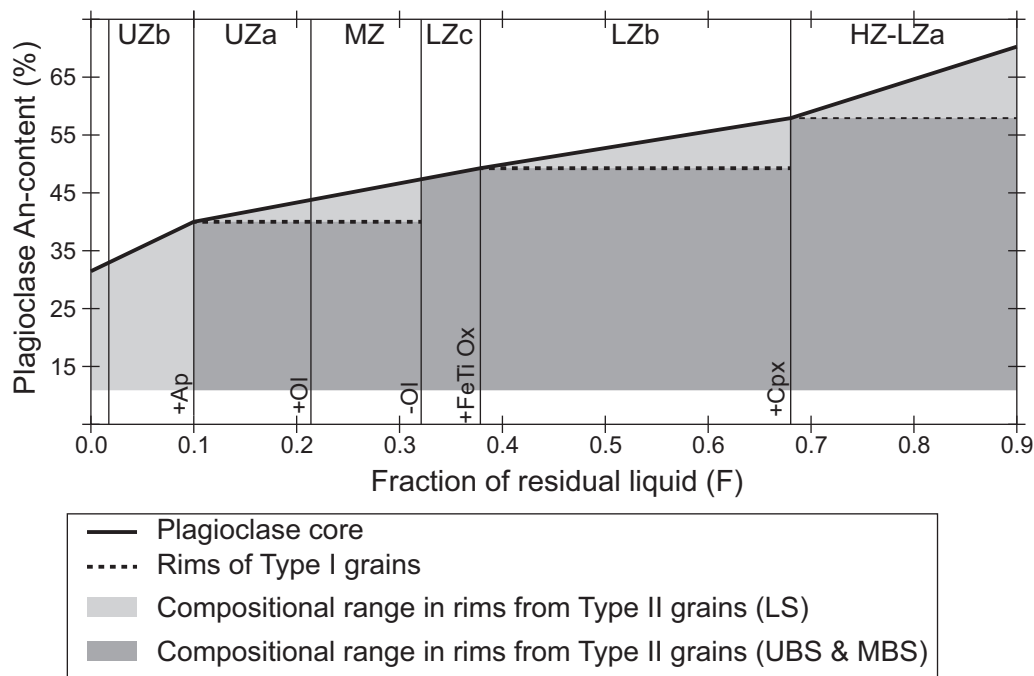
Fig. 13. Schematic representation of the key compositional variations of plagioclase crystals in Skaergaard. The evolution of core and rim compositions (An%) in each unit of the Skaergaard is shown as a function of the residual melt fraction (F) in the magma chamber. The order of mineral appearance is also shown for reference.

MECHANISMS OF CRYSTAL MUSH SOLIDIFICATION: INSIGHTS FROM PLAGIOCLASE

Solidification of the Skaergaard intrusion involved highly effective fractional crystallization of an original ferrobasaltic magma (Hoover, 1989*b*; Nielsen, 2004). This is indicated by the continuous evolution of primocryst compositions throughout the stratigraphy, and the close match between the roof, sidewall and floor cumulate series (e.g. Wager & Brown, 1968; Naslund, 1984; Hoover, 1989*a*; McBirney, 1989; Salmonsen & Tegner, 2013; Fig. 4). However, the precise liquid line of descent of the magma in the chamber is still poorly understood (e.g. Hunter & Sparks, 1987; McBirney & Naslund, 1990; Toplis & Carroll, 1996; Thy *et al.*, 2009*a*; Tegner & Cawthorn, 2010). Large plagioclase cores of constant composition are envisaged as being formed at the top of the crystal mush (i.e. the interface between the mush and the main magma body; McBirney & Noyes, 1979) where strong liquid convection allows the compatible elements to be brought to the crystal–liquid interface whereas the incompatible elements are removed (Morse, 1986, 2008a). The activation energy barrier that has to be overcome for the nuclei to grow and reach a critical size (i.e. leading to the appearance of a new crystal) is relatively small given the presence of pre-existing surfaces for nucleation. Crystal growth is also efficient, even

at relatively low degrees of undercooling (Brandeis & Jaupart, 1986; Pupier *et al.*, 2008).

The evolution of the interstitial liquid within the crystal mush is much less well understood than the evolution of the liquid in the main magma body. When the crystal is buried in the crystal mush owing to the overlying accumulation of new crystals, differentiation and crystallization of the interstitial liquid should result in continuous normal zoning in the outer parts of plagioclase primocrysts, matching their intrusion-scale stratigraphic variation. Although clinopyroxene and olivine should show equivalent variations, these are subject to more rapid diffusive equilibration and hence do not provide such a useful record in the final solidified cumulate.

Mush processes that disrupt fractional crystallization (e.g. infiltration metasomatism, replenishment of interstitial liquid during convection, or fluid flow and dissolution–reprecipitation caused by compaction) disturb this continuous chemical evolution and could potentially produce rocks with normal zoning that do not match the liquidus trend observed in crystal cores, or grains with reverse zoning or, in the extreme, adcumulate rocks with essentially unzoned mineral grains. Some of the plagioclase compositional profiles that we observe in the Skaergaard intrusion clearly deviate from the continuous chemical evolution expected for simple crystallization of a continuously evolving melt, and therefore show that more

complicated processes must have occurred during the solidification of the interstitial liquid. In particular, we need to account for the formation of wide rims of constant composition in Type I grains. It is also crucial to explain why these crystals are more common in the lower parts of the LS, and less common in the UBS and the MBS. Importantly, we must also explain why the rim composition of Type I plagioclase grains is buffered to $An_{56\pm2}$ in LZa (+ LZa* and LZa') independently of the stratigraphic position (Fig. 9), $An_{51\pm1}$ in LZb (+ LZb* and LZb') and $An_{41\pm1}$ from LZc to the lower part of UZa (+ LZc*–UZa* and LZc'–UZa'). It is also of interest to note that the evolution of some minor elements in interstitial plagioclase starts to diverge to that observed in plagioclase cores when the An-content reaches $An56\pm2$ (see fig. 9 in Humphreys, 2011).

A critical observation is that the rim compositions of Type I grains ($An56\pm2$; $An51\pm1$; $An41\pm1$) do not show random patterns but correspond to significant points in the fractionation path of the bulk magma. In detail, $An_{56\pm2}$ is the same within error as the core plagioclase composition at the first appearance of primocryst clinopyroxene in the LS (An_{56-59}; McBirney, 1989), MBS (An_{57-59}; Hoover, 1989a; Namur et al., 2013) and UBS (An_{57-59}; Salmonsen & Tegner, 2013). Additionally, $An_{51\pm1}$ corresponds to the plagioclase primocryst composition at the first appearance of Fe–Ti oxides in the three series (An_{50-52}) and $An_{41\pm1}$ corresponds to that of the first appearance of cumulus apatite (An_{40-41}).

Detailed examination of Ti zoning in interstitial plagioclase shows that new interstitial phases saturate in the mush liquid at an An content similar to that for the appearance of new primocryst phases in the main magma body (Humphreys, 2009). Our new data therefore suggest that the interstitial plagioclase major element composition can locally become buffered each time the interstitial melt adds a new phase to its liquidus assemblage.

ORIGIN OF COMPOSITIONAL BUFFERING OF PLAGIOCLASE RIMS

Based on the primary controls on plagioclase composition, there are several possible causes for the compositional buffering (An content) of rims in Type I plagioclase. These include maintaining the interstitial melt to a constant composition or changing pH_2O, pressure or temperature in the crystal mush.

Despite the control of pressure on plagioclase composition (Longhi et al., 1993; Putirka, 2005) we rule out significant pressure changes during crystallization of the Skaergaard intrusion because the confining pressure changed only slowly during solidification, owing to progressive burial caused by the continuous contemporaneous

eruption of flood basalts (Larsen & Tegner, 2006). Increasing the pH_2O in the magma increases the An content of equilibrium plagioclase (e.g. Panjasawatwong et al., 1995; Putirka, 2005). However, the production of plagioclase rims of constant composition would require pH_2O to increase in such a way that it would exactly counteract the evolution of liquid composition owing to crystallization (i.e. the formation of overgrowths on existing phases and the crystallization of new interstitial crystals). An incommensurately larger increase in pH_2O at any time would result in the formation of reverse rims on plagioclase cores. Such a progressive increase in pH_2O is not supported by any petrographic (e.g. presence of hydrous phases) or geochemical (Humphreys, 2011) evidence, and is also inconsistent with the presence of rims with multiple buffered components in some samples (Fig. 10). We therefore conclude that the most likely cause of the crystallization of constant compositon plagioclase rims is the buffering of the composition of the interstitial melt. This could occur via interstitial liquid mobility or progressive crystal dissolution, or by changes in the thermal regime of crystal mush solidification without addition of any new melt component.

Interstitial liquid mobility

An important matter of debate concerning the crystallization of layered intrusions concerns the mobility of the interstitial liquid within the crystal mush. If interstitial liquid cannot be removed from the mush, in situ crystallization of new interstitial phases (e.g. K-feldspar, apatite, biotite and zircon) will result, incorporating incompatible elements in the evolving liquid consistent with a high 'trapped liquid' fraction (e.g. Tegner et al., 2009). In contrast, if liquid can be physically removed from the mush by compaction (Tegner et al., 2009; McKenzie, 2011), or if rejected components can be efficiently removed from the sites of crystallization by convective flow (e.g. Toplis et al., 2008), adcumulates with low trapped liquid contents can result. Detailed grain-size distribution analysis of cumulate rocks could potentially help to constrain whether adcumulates mostly form as a result of compaction or convective flow (Higgins, 1998). Silicate liquid immiscibility in the crystal mush has also been proposed as a physical mechanism for changing the interstitial liquid composition, by preferential loss of the low-density Si-rich conjugate (Holness et al., 2011).

Compaction of the crystal mush should result in upwards liquid migration, bringing an evolved liquid into contact with overlying crystals that are in equilibrium with more primitive compositions (Irvine, 1980; Humphreys, 2011). This process may have a strong influence on mineral compositions (Irvine, 1980). For the Skaergaard LS, this process should amplify any normal zoning, but it cannot account for the compositional buffering that we see in Type I grains. Moreover, compaction

cannot have been operative either at the roof of the magma chamber (UBS) or on the walls (MBS), where Type I plagioclase grains are also locally present.

Toplis *et al.* (2008) proposed that compositional convection played an important role in the Skaergaard floor cumulates, beginning when the mush liquid became saturated in magnetite. After this point on the liquid line of descent, progressive fractionation results in decreasing liquid density, thus causing gravitational instability within the mush and overturn of the interstitial liquid. Compositional convection exchanges more evolved interstitial liquid with less evolved liquid from the main magma body (or the upper part of the mush), and can therefore keep the melt to a constant composition; we call this 'chemical buffering'. This process has been suggested as acting to buffer the plagioclase rims to An_{51} in cumulate rocks without liquidus Fe–Ti oxides (LZa and LZb), and to produce unzoned grains in cumulates with cumulus Fe–Ti oxides (LZc–UZc; Toplis *et al.*, 2008). Although we agree that compositional convection could lead to effective chemical buffering of the interstitial liquid composition at the saturation of Fe–Ti oxides, and so may have contributed to the formation of some Type I grains in the Skaergaard intrusion, it cannot explain the chemical variability that we observe. This is because saturation of the liquid in interstitial clinopyroxene (at $\sim An_{56-58}$) does not change the liquid density significantly and there is therefore no driving force for compositional convection in LZa. Although Toplis *et al.* (2008) did not describe any grains with rims buffered at $An_{56\pm2}$, our study shows that they are actually a major component of rocks from LZa and equivalent units in the MBS and UBS (Fig. 6; Humphreys, 2011). Furthermore, it has been shown by Humphreys (2011) that the concentration of minor elements such as Ti continuously changes within the rims of Type I grains. Effective compositional convection should, however, result in a buffered concentration of any element in the plagioclase rims (Tait *et al.*, 1984).

A further argument against compositional convection is that it is a gravity-driven process that cannot produce the same results simultaneously on the roof, floor and walls of the magma chamber, as observed in the plagioclase data from the LS, MBS and UBS. Although Type I grains are more common in the LS, they are also present in the wall-rocks (MBS) and at the roof (UBS) of the magma chamber.

It has recently been shown that the interstitial liquid in the Skaergaard crystal mush became immiscible during progressive fractionation (Holness *et al.*, 2011). The coexistence of immiscible conjugate liquids is recorded by the presence of two types of late-stage interstitial intergrowths: those containing quartz and K-feldspar are interpreted as forming from the Si-rich immiscible melt, whereas those rich in Fe–Ti oxides, apatite and pyroxene are interpreted

as forming from the Fe-rich immiscible melt (Holness *et al.*, 2011; Humphreys, 2011). When the two immiscible liquids are in thermodynamic equilibrium, both should crystallize the same plagioclase composition which should then evolve with further differentiation and form normally zoned plagioclase rims. When the two immiscible liquids are sufficiently separated that they lose chemical communication they crystallize plagioclase of a distinctly different composition (Humphreys, 2011). The rims of plagioclase grains forming the walls of Si-rich melt pockets have normal zoning, whereas those forming the walls of Fe-rich melt pockets have a constant composition or even reverse zoning (Humphreys, 2011). The development of two immiscible conjugate liquids, followed by relative movement and/or separation, is therefore not a viable mechanism to produce plagioclase rims of constant composition, unless the relative proportion of the two melts is continuously changing with differentiation. However, there is no reason to suspect that a change in the relative proportion of the two melts would buffer the plagioclase composition to three specific values ($An_{56\pm2}$, $An_{51\pm1}$ and $An_{41\pm1}$). In addition, the residual porosity in rocks from the lower part of the intrusion (HZ–LZa) is likely to have been very low at the onset of immiscibility (<10 vol. %; Humphreys, 2011), and immiscible melts are therefore unlikely to produce the large rims (up to 800 μm wide) of constant composition observed in Type I plagioclase grains, which must have started to form at higher porosity (see below).

Dissolution–reprecipitation in the crystal mush

At low undercoolings, the grain-size distribution of a polydisperse suspension within a liquid evolves under the influence of interfacial energies. The higher free energy of small crystals relative to larger crystals means that the large grains grow at the expense of the smaller. The size effect on solubility equates to an effective superheating of the smaller crystals (Cabane *et al.*, 2005; Simakin & Bindeman, 2008). This is described by the classical theory of Ostwald ripening (Lifshitz & Slyozov, 1961). This process has negligible effect if the crystals are widely separated, particularly for grains larger than a few microns, but occurs at a greater rate when the crystals are touching, as grains may coalesce (Means & Park, 1994; Pupier *et al.*, 2008; Schiavi *et al.*, 2009) or if there is thermal cycling (Simakin & Bindeman, 2008; Mills *et al.*, 2011; Mills & Glazner, 2013). Loss of small grains may also occur by preferential dissolution caused by stress resulting from the pressure of overlying material in the crystal pile (Higgins, 2002; Boorman *et al.*, 2004; Schmidt *et al.*, 2012). Dissolution of small plagioclase grains can feed the growth of larger grains, with the potential to produce compositionally buffered rims and significantly change the original crystal-size distribution (Pupier *et al.*, 2008). An important argument against this being a significant

process for the formation of the buffered Type I rims in the Skaergaard intrusion is that if dissolution results from the stress at the interface between crystals, there is no reason to suspect that dissolution would preferentially occur when the plagioclase An content reaches $An_{56\pm2}$, $An_{51\pm1}$ or $An_{41\pm1}$.

Interface-coupled dissolution of grain boundaries and precipitation of a new phase through the circulation of a fluid phase was recently proposed as a mechanism to produce large plagioclase rims of constant composition (An_{64}) by dissolution of large crystals (An_{80}) in metamorphosed leucograbbro (Svahnberg & Piazolo, 2013). Fluid circulation results in a reaction front migrating into the high-An plagioclase crystals (Svahnberg & Piazolo, 2013) replacing them with a low-An plagioclase, therefore forming a rim around partially resorbed plagioclase grains. However, no clear petrographic or geochemical evidence has been reported for a pervasive and intrusion-wide fluid phase at Skaergaard. Furthermore the buffering at $An_{56\pm2}$, $An_{51\pm1}$ or $An_{41\pm1}$ would apparently require the percolation of three different fluids. We consider this process highly unlikely, especially in the lower part of the LS where the liquids are far too primitive to exsolve a free fluid phase.

Latent heat buffering in a crystal mush

Overproduction of mineral phases during the crystallization of a basaltic melt

The equilibrium proportions of the various liquidus phases of a magma at a given pressure and temperature are fixed by the thermodynamic properties of the system. However, many examples from layered intrusions show that when a new cumulus phase appears its mode is initially higher than expected from cotectic relationships (Morse, 1979a; Wiebe & Snyder, 1993; Tegner et al., 2009; Namur et al.,

2010; Table 3), declining to the expected cotectic proportion within a short stratigraphic distance. This overproduction of a given phase was described by Morse (1979b, 2011) and may be attributed to the supersaturation of the relevant mineral component in the melt, which results in crystallization on metastable extensions of field boundaries (Morse, 1979b). This oversaturation of a new phase may also occur during crystallization from the interstitial melt (Morse, 2011).

Thermodynamic calculations reveal that the crystal productivity [x/T; where x is the amount of crystallization (g) for a given incremental change in temperature (T); e.g. 1°C] at the appearance of a new phase might be up to 10 times higher than under 'normal' conditions (Ghiorso, 1997; Holness et al., 2007, 2009a; Morse, 2011). Crystallization of minerals from a silicate melt is responsible for the release of latent heat of crystallization (ΔH_{fus}), which together with the heat lost through the walls and roof of the magma chamber controls the thermal state of the system and its global cooling rate. Increasing x/T at the appearance of a new phase may therefore result in a non-linear evolution of ΔH_{fus} as a function of temperature (Ghiorso, 1997; Holness et al., 2007, 2013). Such a non-linear evolution of ΔH_{fus} with temperature was observed by Lange et al. (1994) during the melting of basalt and ugandite. Results from this study therefore also point to a non-linear evolution of ΔH_{fus} during the crystallization of a basaltic melt.

In layered intrusions, this process may contribute to keeping the top of the crystal mush close to the liquidus temperature for extended periods (see below). Morse (2011) suggested that this thermal buffering effect contributes to the textural maturation of cumulate rocks. Thermal buffering owing to enhanced release of latent heat at the saturation of a new phase is therefore

Table 3: *Mineral mode at the appearance of cumulus phases in layered intrusions*

	Augite			Fe–Ti oxides			Apatite		
	Appearance F/H	Oversaturation mode	Average mode	Appearance F/H	Oversaturation mode	Average mode	Appearance F/H	Oversaturation mode	Average mode
Skaergaard[1]	0·668/175	27 ± 2	24 ± 2	0·385/742	39 ± 5	24 ± 4	0·097/1620	7·3 ± 1·3	4·4 ± 0·7
Sept Iles[2]	0·72/−3375	29 ± 2	23 ± 3	0·86/−3680	34 ± 8	22 ± 6	0·52/−2575	7·2 ± 0·5	4·6 ± 1·2
Kiglapait[3]	∼0·16/−	40–60	20–30	∼0·08/−	10–40	5–10	∼0·05/−	8–12	1–5
Newark Island[4]	−/1000	25–30	15–20	−/1300	16–25	8–10	−/2500	8·5	1

[1]Tegner et al. (2009).
[2]Namur et al. (2010).
[3]Morse (1979a).
[4]Wiebe & Snyder (1993).
F, fraction of residual melt; H, stratigraphic height (m).

considered as an explanation for the stepwise evolution of clinopyroxene–plagioclase–plagioclase dihedral angles (Φ_{cpp}) at the appearance of clinopyroxene, Fe–Ti oxides and apatite in fractionated layered intrusions (e.g. Skaergaard, Bushveld and Sept Iles; Holness *et al.*, 2007, 2013). Enhanced release of latent heat at the appearance of a new phase, as opposed to a uniform distribution of latent heat across the liquidus–solidus interval (Ghiorso, 1991), is also thought to be an efficient process acting to thermally homogenize large silicic magma chambers (Huber *et al.*, 2009) and thick lava flows (Settle, 1979).

Modelling the crystal productivity and latent heat production in basalt

As illustrated above, the saturation of new phases in a basaltic melt has the potential to significantly change the temperature derivative of ΔH_{fus} and therefore to exert a primary control on the cooling rate of a magma body. We used thermodynamic modelling to put quantitative constraints on the ΔH_{fus} vs T path of a Skaergaard-related magma and use these results to discuss the cooling rate of a gabbroic crystal mush.

We used the most recent alphaMELTS calibration of the MELTS thermodynamic calculator (Ghiorso & Sack, 1995; Smith & Asimov, 2005) to calculate the thermodynamic properties of some representative basaltic and ferrobasaltic melts and to evaluate the heat budget of crystallizing basaltic magma in a shallow magma chamber such as the Skaergaard intrusion. We used a primitive mid-ocean ridge basalt (MORB) composition (Ghiorso, 1997) and four possible compositions of the Skaergaard parental magma (Toplis & Carroll, 1996; Nielsen, 2004; Thy *et al.*, 2009*a*; Tegner & Cawthorn, 2010; Table 4). Calculations were performed to simulate a process of fractional crystallization at 1 kbar along the quartz–fayalite–magnetite (QFM) oxygen fugacity buffer. Calculated liquid lines of descent of these melts are shown in Fig. 14a. The accuracy of MELTS was assessed by comparing predicted liquid lines of descent for various ferrobasaltic provinces with published suites of whole-rock compositions (Fig. 14b). We also compared MELTS predictions for mineral compositions and cotectic proportions with rocks from the Skaergaard intrusion as well as theoretical models (Thy *et al.*, 2009*a*) and experimental results (Toplis & Carroll, 1995), and found that MELTS predicts these parameters reasonably accurately (Table 4).

Crystallization of basaltic melts results in peaks in crystal productivity at the appearance of each cumulus phase (Fig. 15; Table 4). This enhanced production of crystals at the saturation of a new phase is due to the liquidus slope flattening temporarily when the new phase appears on the liquidus (Wyllie, 1963; Morse, 2011). The increasing crystal productivity results in an increasing production of latent heat of crystallization [$(\Delta H_{fus}/\Delta T$; J g^{-1} K^{-1}; Ghiorso, 1997; Morse, 2011; Holness *et al.*, 2013; Fig. 15],

which we calculated following Ghiorso & Carmichael (1985) and Lange *et al.* (1994):

$$\Delta H_{fus} = (H_T + \Delta_T) - \Delta T C_p \qquad (2)$$

where H is enthalpy (J g^{-1}), T is temperature (K) and C_p is the specific heat (J g^{-1} K^{-1}). The temperature derivative of ΔH_{fus} generally decreases with T (or F; fraction of remaining melt in the magma chamber) at a rate dependent on the stable liquidus assemblage. This trend is punctuated by significant jumps in $\Delta H_{fus}/\Delta T$ at the appearance of a new liquidus phase. The intensity of this jump mostly depends on the thermodynamic properties (e.g. enthalpy of fusion) and the cotectic proportion of the phase that starts crystallizing.

Implications for crystal mush cooling

When compared with the total enthalpy budget of the system, the latent heat of crystallization represents *c.* 80% of the heat budget during most of the magmatic history (Holness *et al.*, 2007, 2009*a*; Morse, 2011). The appearance of a new cumulus phase, however, increases the latent heat contribution to the total heat budget of the system. This therefore has the potential to decrease the global cooling rate of the magma because most of the heat dissipated through the country-rocks is latent heat (Cashman, 1993; Dunbar *et al.*, 1995; Higgins, 1998; Morse, 2011). For convenience, we can define the specific cooling rate as the inverse of the crystal productivity (T/x). It is evident from Fig. 15 (upper panels) that the cooling rate diminishes discontinuously at the appearance of a new phase on the liquidus. The specific cooling of the bulk magma chamber could therefore approach zero during the peaks of crystal productivity (Morse, 2011). In a large, homogeneous, convecting magma chamber such as Skaergaard, the enhanced latent heat production presumably does not play any significant role in the global cooling of the bulk magma chamber. This is because crystallization dominantly occurs in slightly undercooled boundary layers against the walls (Brandeis *et al.*, 1984; Worster *et al.*, 1990; Morse, 2008*a*), while the bulk magma body is above the liquidus temperature (McBirney & Noyes, 1979; Brandeis & Jaupart, 1986; Morse, 1986, 2008*a*). At any stage of crystallization the volume of crystals produced is relatively small compared with the volume of liquid in the magma chamber and the extra latent heat is quickly dissipated within the whole convecting magma body and cannot therefore counteract the heat lost through the country rocks (see below).

In contrast, enhanced release of latent heat might play an important role for the comparatively smaller volume of magma within and immediately adjacent to the crystal mush and potentially maintain it under near-isothermal conditions (Brandeis *et al.*, 1984; Higgins, 1998; Holness *et al.*, 2007; Morse, 2011). We used the MELTS results

Table 4: Results of MELTS calculations for the fractional crystallization of a basalt and comparison with published models

Composition	Unit	Ghiorso (1997) MELTS model	Toplis & Carroll (1996) MELTS model	Nielsen (2004) MELTS model	Tegner & Cawthorn (2010) MELTS model	Thy et al. (2009a) MELTS model	Toplis & Carroll (1995) Experiments	Thy et al. (2009a) Modelling	Natural rocks Layered Series
SiO_2	wt %	48·68	48·70	47·91	47·61	47·62	48·8	47·62	49·69[1]
TiO_2	wt %	1·01	2·90	3·09	3·39	2·87	2·9	2·87	2·66
Al_2O_3	wt %	17·64	14·90	13·80	13·50	13·73	14·9	13·73	13·51
FeO_t	wt %	8·39	13·10	15·43	15·84	15·24	13·1	15·24	13·11
MnO	wt %		0·24	0·24	0·24	0·25		0·25	0·22
MgO	wt %	9·10	6·50	6·13	6·15	6·33	6·5	6·33	6·61
CaO	wt %	12·45	10·90	10·16	9·97	10·62	10·9	10·62	10·18
Na_2O	wt %	2·65	2·70	2·57	2·59	2·45	2·7	2·45	2·37
K_2O	wt %	0·03	0·30	0·40	0·37	0·42	0·3	0·42	0·56
P_2O_5	wt %	0·08	0·30	0·28	0·34	0·26	-	0·26	0·22
fO_2	(ΔFMQ)	0	0	0	0	0	0	0	~0[2]
Pressure	kbar	1	1	1	1	1	0·001	0·001	~1-2[3]
Liquidus temp.	°C	1225	1165	1155	1151	1161	1158	1162	
Lowest temp.	°C	1000	1000	1000	1000	1000	1057	1000	
Mineral compositions									
Plagioclase	An%	82-35	71-39	70-41	69-42	72-42	71-43	LZa-UZb: 70-45	LZa-UZb: 67-40[4]
Olivine	Fo%	87-71	70-49	69-46	67-45	68-45	75-59	LZa-UZb: 66-40	LZa-UZb: 66-40
Clinopyroxene	Mg#%	84-56	79-62	78-40	76-50	78-49	75-53	LZa-UZb: 77-46	LZa-UZb: 75-50
Sequence of crystallization									
First liquidus phases	-	Plag	Plag, Ol	Plag	Plag	Plag, Ol	Plag, Ol	Plag, Ol	Plag, Ol
Arrival (T)/Arrival (F) of other phases									
Olivine	°C/-	1219/0·95	-	1153/0·98	1142/0·97	-	-	-	-
Clinopyroxene	°C/-	1201/0·81	1150/0·90	1142/0·82	1127/0·85	1135/0·82	1135/0·75	1150/0·85	1124[5]/0·70[6]
Fe-Ti oxides	°C/-	1117/0·31	1108/0·63	1104/0·53	1104/0·54	1100/0·49	~1100/0·50-0·30	1099/0·56	1085-1120/0·41
Apatite	°C/-	1009/0·11	1030/0·24	1016/0·24	1028/0·26	1016/0·23	-	1038/0·30	1035-1060/0·11
Cotectic proportions									
Plag	wt %	100	-	100	100	-	-	-	-
Plag/Ol	wt %	74/26	67/33	65/35	73/27	68/32	70/30[7]	73/27[8]	80/20[9]
Plag/Ol/Cpx	wt %	48/11/41	50/22/28	54/20/26	52/10/38	48/25/27	48/12/40	46/9/45	52/6/42
Pl/Ol/Cpx/FeTiOx	wt %	50/0/32/18	51/7/24/18	50/10/17/23	42/0/35/23	46/10/24/20	37/11/43/9	39/7/36/18	39/5/36/20
Pl/Ol/Cpx/FeTiOx/Ap	wt %	52/0/26/21/1	52/12/17/14/5	56/5/13/19/7	52/0/26/17/5	53/11/14/17/5	-	-	41/23/22/9/5

Ratio of crystal productivity (g °C^{-1}) before and after the appearance of a new phase and range of temperature of 'high' crystal productivity (MELTS calculations)[10]

(continued)

Table 4: Continued

Composition	Unit	Ghiorso (1997) MELTS model	Toplis & Carroll (1996) MELTS model	Nielsen (2004) MELTS model	Tegner & Cawthorn (2010) MELTS model	Thy et al. (2009a) MELTS model	Toplis & Carroll (1995) Experiments	Thy et al. (2009a) Modelling	Natural rocks Layered Series
Olivine	–/°C	3·2/–[11]	–	4·1/–	2·2/–	–	–	–	–
Clinopyroxene	–/°C	1·7/20	7·4/30	13·2/20	3·8/17	8·1/–	–	–	–
Fe–Ti oxides	–/°C	2·2/25	16·9/15	34·3/25	34/20	29·2/25	–	–	–
Apatite	–/°C	1·1/10	1·3/8	1·4/15	1·3/10	1·3/13	–	–	–
Ratio of $\Delta H_{fus}/\Delta T$ (J g^{-1} K^{-1}) before and after the appearance of a new phase and range of temperature of 'high' $\Delta H_{fus}/\Delta T$ (MELTS calculations)[12]									
Olivine	–/°C	3·6/–[13]	–	0/–	2·1/–	–	–	–	–
Clinopyroxene	–/°C	1·7/20	11·8/30	5·1/30	4·1/10	4·8/–	–	–	–
Fe–Ti oxides	–/°C	2·0/22	15·5/15	24·7/15	23·7/14	20·6/20	–	–	–
Apatite	–/°C	1·1/5	1·2/7	1·3/10	1·2/7	1·3/10	–	–	–

[1]Parental magma composition from Hoover (1989b).
[2]Oxygen fugacity conditions from Toplis & Carroll (1995) and Thy *et al.* (2009a).
[3]Pressure from Larsen & Tegner (2006).
[4]Mineral compositions from McBirney (1989).
[5]Temperature from Thy *et al.* (2009b) and Morse (2008b).
[6]Residual liquid proportion from Tegner *et al.* (2009).
[7]Proportions from Toplis & Carroll (1996).
[8]Proportions from Thy *et al.* (2006).
[9]Proportions from Tegner *et al.* (2009).
[10]The ratio of crystal productivity before and after the appearance of a new liquidus phase is calculated using the highest crystal productivity value after the change in liquidus assemblage and the lowest crystal productivity value immediately preceding the change. The temperature range corresponds to cooling needed to return to a crystal productivity per temperature increment identical to that observed immediately before the appearance of the new phase.
[11]– indicates that a new phase saturates before the crystal productivity 'jump' owing to the saturation of the previous phase returns to the background value immediately before the jump.
[12]The ratio of $\Delta H_{fus}/\Delta T$ before and after the appearance of a new liquidus phase is calculated using the highest $\Delta H_{fus}/\Delta T$ after the change in liquidus assemblage and the lowest $\Delta H_{fus}/\Delta T$ immediately preceding the change.
[13]– indicates that a new phase saturates before the $\Delta H_{fus}/\Delta T$ 'jump' owing to the saturation of the previous phase returns to the background value immediately before the jump.
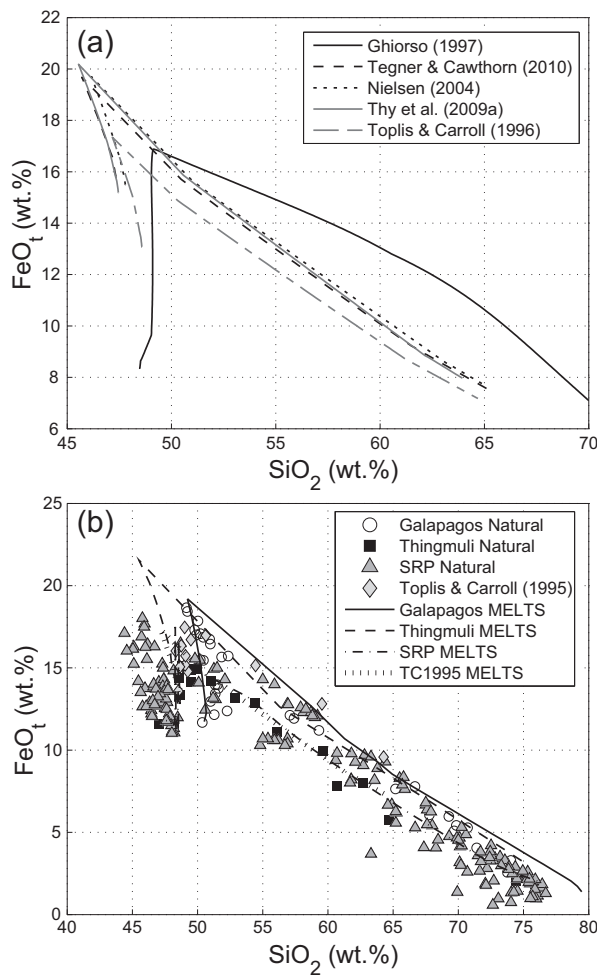
Fig. 14. (a) MELTS predicted liquid lines of descent for a MORB starting composition (Ghiorso, 1997) and various Skaergaard-like magma compositions (Toplis & Carroll, 1996; Nielsen, 2004; Thy *et al.*, 2009a; Tegner & Cawthorn, 2010). MELTS calculations were performed at 1 kbar and QFM conditions. (b) Comparison between MELTS calculated liquid lines of descent for some ferrobasaltic provinces [Galapagos; Thingmuli; Snake River Plain (SRP)] and bulk-rock compositions of erupted lavas. A comparison between liquids predicted by MELTS and experimental liquids for a Skaergaard-like magma (Toplis & Carroll, 1995) is also shown. Bulk-rock data are from Carmichael (1964), Byerly *et al.* (1976) and Andrews *et al.* (2008).

presented above to estimate how the crystallization of a new phase influences the thermal regime of a crystal mush. Calculations are based on three important assumptions, as follows.

(1) The mush liquid is cooling by losing enthalpy through the country-rocks at a constant rate (e.g. Morse, 1986; Spera & Bohrson, 2001). If the latent heat of crystallization stays constant, the thermal evolution of the magma body can therefore be expressed as a constant cooling rate, R (°C a^{-1}), which we estimated to be in the range 0·01−0·001°C a^{-1} (Kuritani *et al.*, 2007; Morse, 2011).
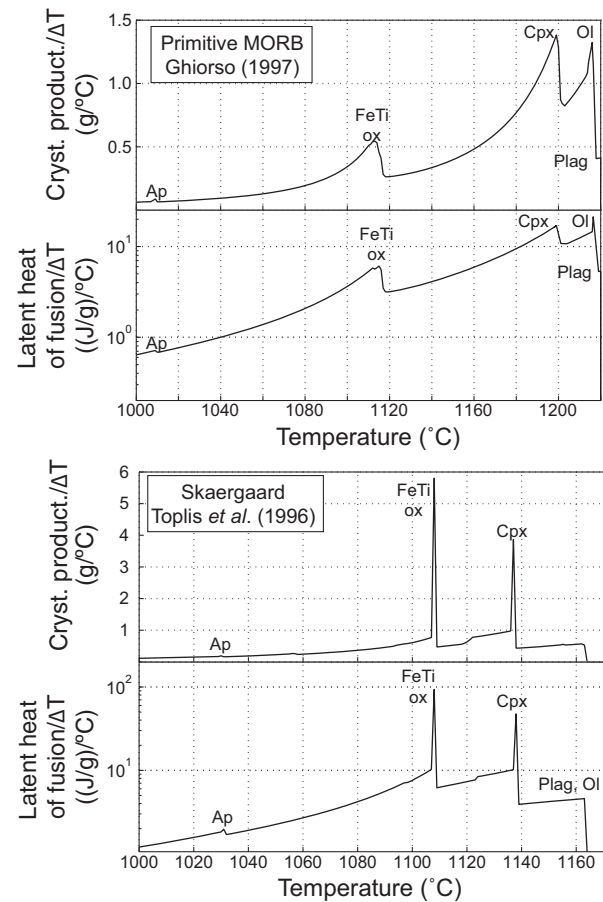
Fig. 15. Diagrams showing the evolution of crystal productivity (amount of crystallization for a given incremental change in temperature; 1°C) and the latent heat of crystallization (normalized to the mass of remaining magma) as a function of temperature (i.e. progressive fractionation of the starting liquid compositions). Results are shown for a primitive MORB starting composition (Ghiorso, 1997) and a Skaergaard-related magma (Toplis & Carroll, 1996). Results on other Skaergaard-related magmas are given in Table 4 (Nielsen, 2004; Thy *et al.*, 2009a; Tegner & Cawthorn, 2010). It should be noted that the crystal productivity and latent heat curves show well-defined spikes at the appearance of each successive phase. Plag, plagioclase; Ol, olivine; Cpx, clinopyroxene; FeTi ox, Fe–Ti oxides; Ap, apatite.

(2) The whole volume of interstitial liquid becomes saturated in the new phase exactly at the same time, so the latent heat of crystallization is homogeneously distributed within the liquid mass.

(3) We consider a temperature range of 190°C between the liquidus temperature and the solidus temperature (e.g. 1170–980°C; Toplis & Carroll, 1995; Thy *et al.*, 2009b; Charlier & Grove, 2012).

Based on these assumptions and considering a crystal mush initially made up of liquid (40 vol. %) + plagioclase and olivine, we can use the thermodynamic data predicted by MELTS (e.g. enthalpy of fusion of the parental basalt; ∼1 × 10^6 J kg^{-1}; specific heat ∼1·3 × 10^3 J kg^{-1} K^{-1}) and

equation (2) to calculate that the mushy layer must conductively lose ~10 000 J kg^{-1} to the country-rocks to be cooled by 1°C. Depending on the estimated cooling rate (e.g. 0·001–0·01 °C a^{-1}; Morse, 2011), we can therefore calculate that the jumps in the latent heat output at the appearance of a new phase (Fig. 15) can maintain the mush liquid at near-isothermal conditions for times in the range of 42–420 years at the appearance of interstitial clinopyroxene, 220–2200 years at the appearance of Fe–Ti oxides and 4–40 years at the appearance of apatite (Fig. 16a). These values are lower by a factor of 2 than those suggested by Morse (2011), who used the cotectic proportions and thermodynamic properties of a liquid which is significantly different to the Skaergaard parent magma.

Adcumulus growth in the crystal mush

The calculations presented above indicate that the mush liquid may stay at near-isothermal conditions (very low cooling rate) temperature at several points during its solidification owing to episodes of enhanced release of latent heat at the saturation of each new phase. However, the more fully solidified cumulates far from the solidification front continue to lose heat by conduction through the walls, roof and floor of the magma chamber. This provides a driving force for further crystallization in the crystal mush, even at a low degree of undercooling (Morse, 2008a, 2011). The thermodynamic force for crystallization is, however, small and solidification mostly occurs through crystal growth on existing grains (i.e. formation of rims) with a very minor formation of new grains (Brandeis *et al.*, 1984; Pupier *et al.*, 2008). Considering a typical growth rate for plagioclase (e.g. 10^{-11}–10^{-12} cm s^{-1}; Cashman, 1993; Pupier *et al.*, 2008), we calculated that plagioclase rims (i.e. overgrowths) ranging in size from *c.* 10 to 1000 μm may form on the time-scales we have established for the periods of isothermal conditions (Fig. 16b). However, their constant composition still needs to be discussed.

The local enhanced release of latent heat (Fig. 17a) at the saturation of a new interstitial phase is capable of thermally buffering the interstitial melt (Fig. 17b) but also has two additional effects, as follows.

It progressively decreases the degree of undercooling, which tends to zero (Fig. 17c; Hort & Spohn, 1991a). Reducing the degree of undercooling (Brandeis & Jaupart, 1986; Higgins, 1998; Couch *et al.*, 2003) diminishes the extent of disequilibrium between the liquid and associated plagioclase (Hort & Spohn, 1991a, 1991b), which potentially increases the An content of plagioclase growing from any given liquid composition (Loomis, 1982; Muncill & Lasaga, 1987). We used thermodynamic modelling of plagioclase–liquid equilibrium [equation (28) of Namur *et al.* (2012)] to calculate the effect of changing the extent of undercooling (up to 20°C in increments of 1°C) on the plagioclase composition in equilibrium with the
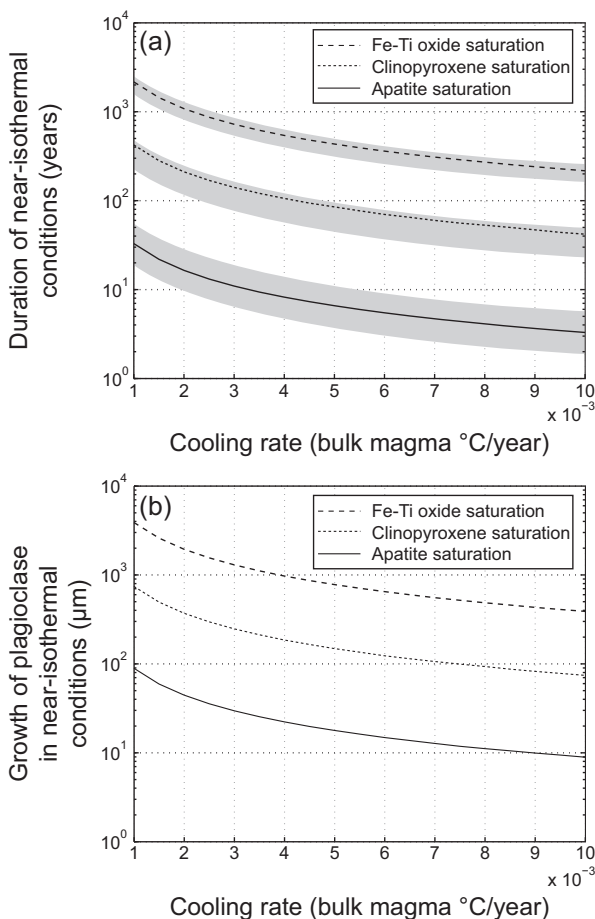

Fig. 16. (a) Estimation of the time spent at isothermal (or near-isothermal) conditions for a given volume of magma when it becomes saturated in a new cumulus phase. We calculated the evolution of melt temperature as a function of time ($\Delta H/\Delta T$) and considered a liquid density of 2·75 g cm^{-3}. We assumed that the system is losing enthalpy to the country-rocks at a continuous rate ($\Delta H/\Delta t$ is constant). This rate was calculated using the global enthalpy of the system (calculated from MELTS; see Table 4) and cooling rates suggested by Morse (2011) for the Skaergaard magma chamber (0·001–0·01 °C a^{-1}). This diagram shows the period of time during which the whole system (i.e. homogeneous nucleation and crystal growth in the whole magma body) or the top of the crystal mush (i.e. *in situ* crystallization) may stay under near-isothermal conditions at the appearance of clinopyroxene, Fe–Ti oxides and apatite. Lines (including the dashed lines) show the results with the average value of latent heat of crystallization at the saturation of a new phase calculated from MELTS data using the parental melts listed in Table 4. Grey fields represent the range of years spent at isothermal conditions calculated using lowest and highest values of latent heat of crystallization calculated from MELTS data using the parental melts listed in Table 4. (b) Size of the crystals that may be reached by crystal growth under near-isothermal conditions at the appearance of clinopyroxene, Fe–Ti oxides and apatite. Crystal growth rate is from Cashman (1993).

Skaergaard parental magma. This analysis reveals that the plagioclase composition changes by 0·1% An when the amount of undercooling is decreased by 1°C. It therefore acts in an opposite way to differentiation, and so might contribute, at least in part, to maintaining
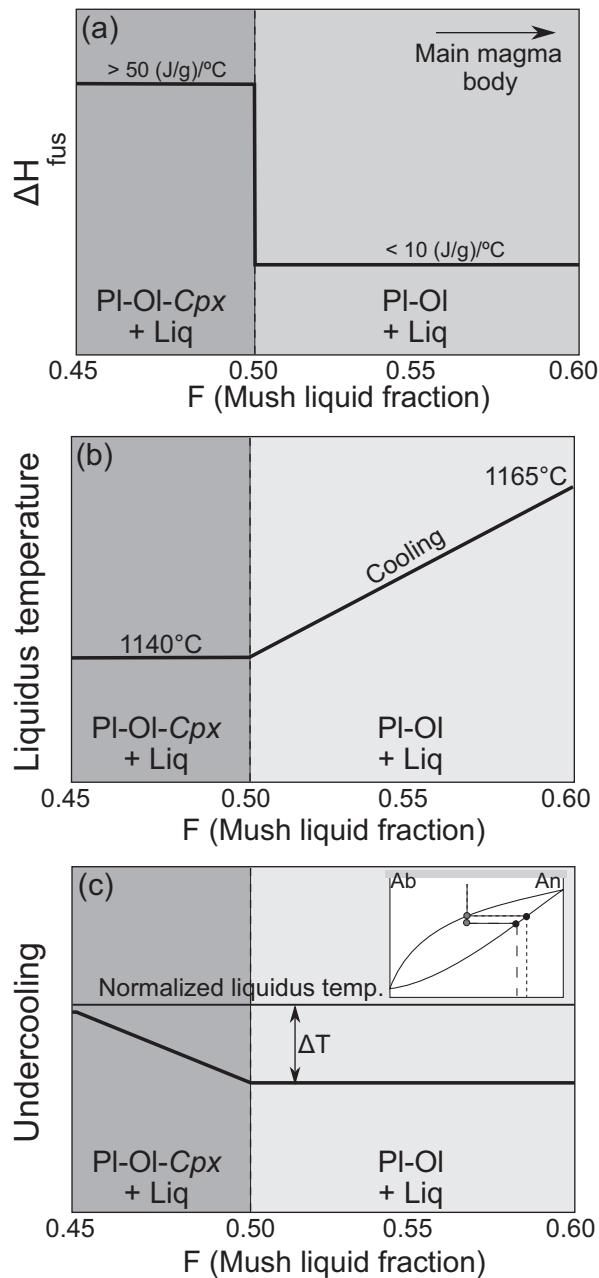
Fig. 17. Schematic illustration of the thermal history of an LZa crystal mush (at the appearance of interstitial clinopyroxene). An initial mush porosity of 0·6 is assumed (see Jerram *et al.*, 2003) and we consider that the mush liquid fraction decreases only owing to crystallization of interstitial phases and formation of mineral overgrowths (e.g. no liquid is expelled by crystal mush compaction). We also consider that the composition of the interstitial liquid is not altered by compositional convection or any other process. The part of the mush on the right side ($F = 0·6$–$0·5$) contains cumulus olivine and plagioclase and the interstitial liquid crystallizes plagioclase and olivine, whereas the mush on the left side ($F = 0·5$–$0·45$) contains cumulus olivine and plagioclase and the interstitial liquid crystallizes plagioclase, olivine and clinopyroxene. We assume that the liquid within the mush has initially ($F = 0·6$) the composition of the Skaergaard parent magma and has a liquidus temperature of 1165°C. The mush liquid is considered to follow the same differentiation path as the main magma

a constant plagioclase composition (Chistyakova & Latypov, 2012).

It allows near-equilibrium, adcumulus, crystal growth (Wager *et al.*, 1960; Morse, 1986, 2008*a*; Hort & Spohn, 1991*a*). Where equilibrium is maintained between the growing crystals and the liquid, adcumulus growth can occur with the potential to produce rims of constant composition such as those observed in the Skaergaard intrusion (Morse, 2008*a*). Crystal growth, however, depletes the melt in elements compatible in plagioclase, whereas incompatible elements are enriched. This results in the formation of a compositional boundary layer around the crystals (Albarède & Bottinga, 1972) that needs to be erased to keep a liquid of constant composition at the crystal–liquid interface. Following Morse (2011), this can be achieved by diffusion alone as long as the accumulation rate at the top of the crystal mush is lower than 4–6 cm a^{-1}. A higher accumulation rate would hamper the connection between the mush liquid and the main magma body. For the Skaergaard intrusion the estimated range of crystal accumulation rates is 1–4 cm a^{-1} (Morse, 2011), indicating that diffusion is fast enough the keep the crystal–liquid interface at a constant composition when the mush liquid is isothermal. This is confirmed by the very high diffusivity of Na$^+$ (*c.* 1×10^{-9} m^2 s^{-1}), and diffusion of Ca^{2+} is also relatively fast (*c.* 1×10^{-11} m^2 s^{-1}) and similar to, or slightly faster than, that of other major elements (Supplementary Dataset 5). Short length-scale convection owing to Na diffusion (Bindeman & Davis, 1999) may also contribute to maintaining a constant composition liquid at the interface with plagioclase crystals and may therefore contribute to the extent of adcumulus growth (Morse, 2008*a*, 2011).

Summary of the crystallization history of Type I plagioclase grains

Crystallization of Type I plagioclase grains starts by nucleation and crystal growth at the interface between the

Fig. 17 Continued
body (Humphreys, 2009). Following the results of MELTS calculations (see Table 4), clinopyroxene therefore starts crystallizing as an interstitial phase at 1140°C when the mush porosity is 0·5. (a) Change in total enthalpy of fusion per °C as a function of the mush liquid fraction. It should be noted that the latent heat of crystallization is significantly higher in that part of the mush that contains interstitial clinopyroxene than in the mush with plagioclase and olivine only. These values of latent heat of crystallization should be compared with those in Table 4 for additional information. (b) Change of melt liquidus temperature with depth (or decreasing liquid fraction) in the mush. It should be noted that the liquid in the mush containing interstitial clinopyroxene is buffered to its liquidus temperature. (c) Schematic representation of the change of the degree of undercooling. Undercooling progressively decreases with time in the mush containing clinopyroxene. Results of changing the degree of undercooling on equilibrium plagioclase composition are schematically shown in the albite–anorthite loop (inset). The dotted trajectory shows the equilibrium plagioclase composition (no undercooling) and the dashed trajectory shows the plagioclase composition produced from the same melt with an undercooling of *c.* 10°C.
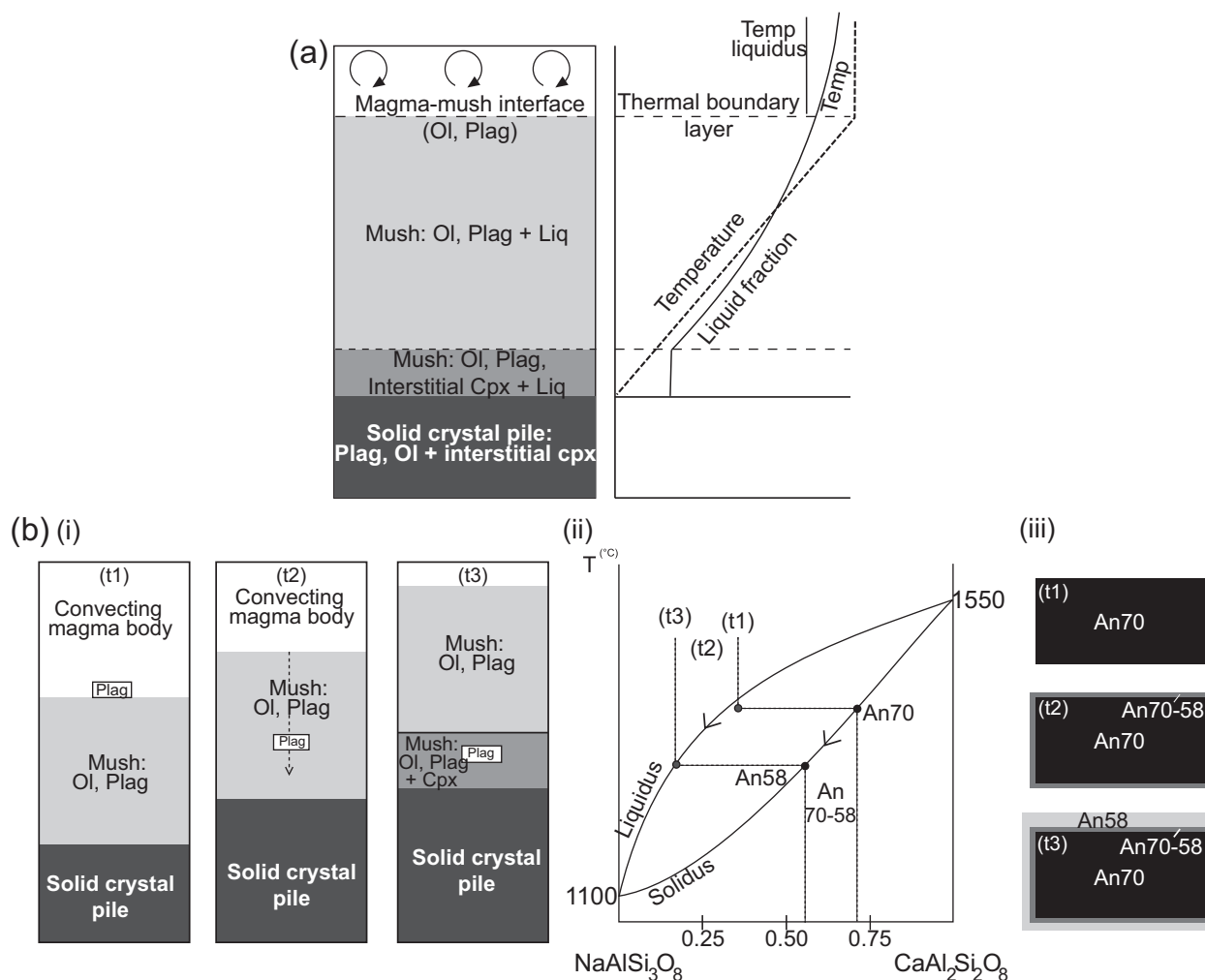
Fig. 18. Structure of the plagioclase, olivine and liquid crystal mush at the appearance of interstitial clinopyroxene and its effect on plagioclase crystallization history. (a) The schematic diagram on the left represents a subsection from the bottom of the magma chamber. From base to top it shows a first layer representing the upper part of the fully crystallized cumulate pile with cumulus plagioclase and olivine + interstitial clinopyroxene, then the crystal mush (liquid + crystals) and finally the lowermost part of the convecting main magma body (above the magma–mush interface). The relative thicknesses of the various units have no significance and were chosen to focus on the crystal mush. The liquid within the mush is evolving in composition downwards so that the liquid in the lower part is saturated in olivine, plagioclase and clinopyroxene, whereas the liquid in the upper part is saturated in olivine and plagioclase only. The liquid temperature within the mush increases upwards. Following Worster (1997) and Morse (2008*a*) the temperature of the liquid within the main magma body is slightly above the liquidus so that no nucleation and crystal growth occur within the main magma body. The porosity within the mush decreases downwards (for simplicity this decrease is considered as evolving linearly with depth) owing to crystallization of interstitial phases and overgrowth on cumulus phases. The latent heat release is higher in the lower part of the mush than in the upper part, which results in maintaining the liquid in the lower part of the mush at its liquidus temperature (see text for details). (b) Crystallization history of a plagioclase grain located within the lower part of the mush and representation on the compositional path of plagioclase on the albite–anorthite loop. At t1, (i) initial nucleation (owing to slight undercooling) occurs at the top of the mush; (ii) the plagioclase composition in equilibrium with the melt is An_{70}; (iii) crystal growth produces a large plagioclase crystal of constant composition (An_{70}). At t2, (i) the plagioclase crystal is buried within a mush containing a liquid saturated in olivine and plagioclase. The dotted arrow represents the evolution of plagioclase burial depth within the mush through time (ii–iii). Differentiation of the mush liquid results in the formation of a plagioclase mantle with decreasing An content (An_{70-58}). At t3, (i) the plagioclase crystal is at the bottom of the mush, which contains a liquid saturated in olivine, plagioclase and clinopyroxene and which stays under isothermal conditions for an extended period of time (possibly >1000 years; see text for explanation); (ii, iii) equilibrium crystallization under isothermal conditions produces a rim of constant composition (An_{58}).

crystal mush and the main magma body, where the liquid is at the liquidus temperature or slightly undercooled (Fig. 18a). This first step results in the formation of a large core of constant composition (e.g. An_{70}; t1 in Fig. 18b).

The crystal is then progressively buried in the developing mushy layer in which the liquid is initially saturated in the same phases as those crystallizing from the main magma body (i.e. olivine and plagioclase; t2 in Fig. 18b).

At this stage, differentiation and crystallization of the interstitial melt produces rims of decreasing An content around the crystal cores (e.g. $An_{70–58}$) owing to changes in melt composition and decreasing temperature. When the mush liquid becomes sufficiently evolved, it may start crystallizing a new phase (e.g. clinopyroxene; t3 in Fig. 18b). The enhanced release of latent heat associated with the appearance of the new phase maintains, at least locally, the mush liquid under isothermal conditions, and diffusion of chemical species maintains a constant liquid composition at the crystal–liquid interface. This step produces rims of constant composition (e.g. An_{58}) on the plagioclase crystals. If the process goes to completion, the residual porosity goes to zero isothermally.

PLAGIOCLASE ZONING IN THE SKAERGAARD INTRUSION
Influence of mush liquid fraction

Thermal buffering of the mush is envisaged as an efficient way to produce adcumulus growth, which can produce the rims of constant composition that we see in Type I grains. On the other hand, simple crystallization of a melt with continuously evolving composition is capable of producing the rims with normal zoning observed in Type II grains, whereas compaction of the mush (Tegner *et al.*, 2009) or efficient compositional convection can account for the formation of the unzoned Type III grains. As illustrated in Fig. 6, each type of plagioclase grain (Type I, Type II and Type III) has its own stratigraphic distribution in the Skaergaard intrusion. Type I grains are mostly abundant in the lower part of the LS, but are present up to UZa, whereas Type III grains dominate the upper part of the LS. Type II grains are mostly observed in the MBS and UBS. These three series show the same succession of cumulate rocks but have contrasted interstitial liquid fractions (Fig. 19). The Appendix gives the details of the calculation procedure [see Table 2 and Tegner *et al.* (2009), Namur *et al.* (2013) and Salmonsen & Tegner (2013) for details of the bulk-rock compositions and analytical methods]. The contrasted stratigraphic distribution of the different types of plagioclase grains, together with the variable interstitial liquid fractions in the different series of the Skaergaard intrusion, suggests that this parameter may exert a primary control on the dominant type of plagioclase zoning in each sample. This may originate from (1) the potential control of the liquid fraction on the degree of supersaturation of any mineral component in the melt and therefore the temperature derivative evolution of ΔH_{fus} upon solidification (Morse, 1979b, 2011) or (2) the control of the liquid fraction (i.e. porosity) on the degree of liquid mobility and the efficiency of heat advection in the crystal mush (McKenzie, 1984; Tait *et al.*, 1984; Huber *et al.*, 2009; Namur & Charlier, 2012).
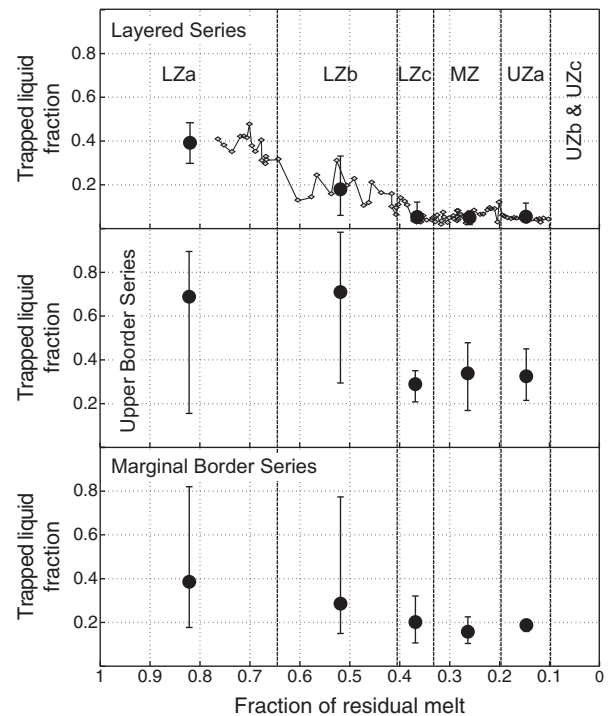

Fig. 19. Calculated average (filled black circle) and range (vertical lines) of the interstitial liquid fraction in rocks from each zone of the Layered Series, Upper Border Series and Marginal Border Series. Calculations are based on whole-rock P_2O_5 content and cannot therefore be performed for the zones containing cumulus apatite (UZb and UZc). Grey diamonds represent the interstitial liquid fraction in single samples from the Layered Series (see Tegner *et al.*, 2009). Bulk-rock analyses are from Tegner *et al.* (2009), Namur *et al.* (2013), Salmonsen & Tegner (2013) and unpublished MBS data from the sections KR-01 and KR-03 (see Fig. 1). (See the Appendix for details on the calculation procedure.)

We consider a magma chamber developing mushy crystal layers on its margins (Fig. 20a). As above, we consider that the system needs to lose *c.* 10 000 J kg^{-1} of magma to cool the mush liquid temperature by 1°C. This is illustrated in a simple system saturated in two phases (e.g. plagioclase and olivine). At t1 in Fig. 20b, no crystallization occurs. At t2, crystallization of interstitial olivine and plagioclase has occurred and the system has cooled slightly (e.g. 1°C). We now consider two cases when a new interstitial phase appears on the liquidus, as follows.

(1) The new phase (e.g. clinopyroxene) saturates in the whole volume of mush liquid. As discussed above, the saturation of a new phase produces a significant increase in the latent heat of crystallization. We used MELTS to investigate whether or not the fraction of liquid in the mush exerts a primary control on the heat release in the system (Supplementary Dataset 6). We ran calculations (1400–1000°C; 1kbar) on nine MORB (or residual liquids from MORB) starting compositions (Ghiorso, 1997; Kamenetsky *et al.*, 2000)
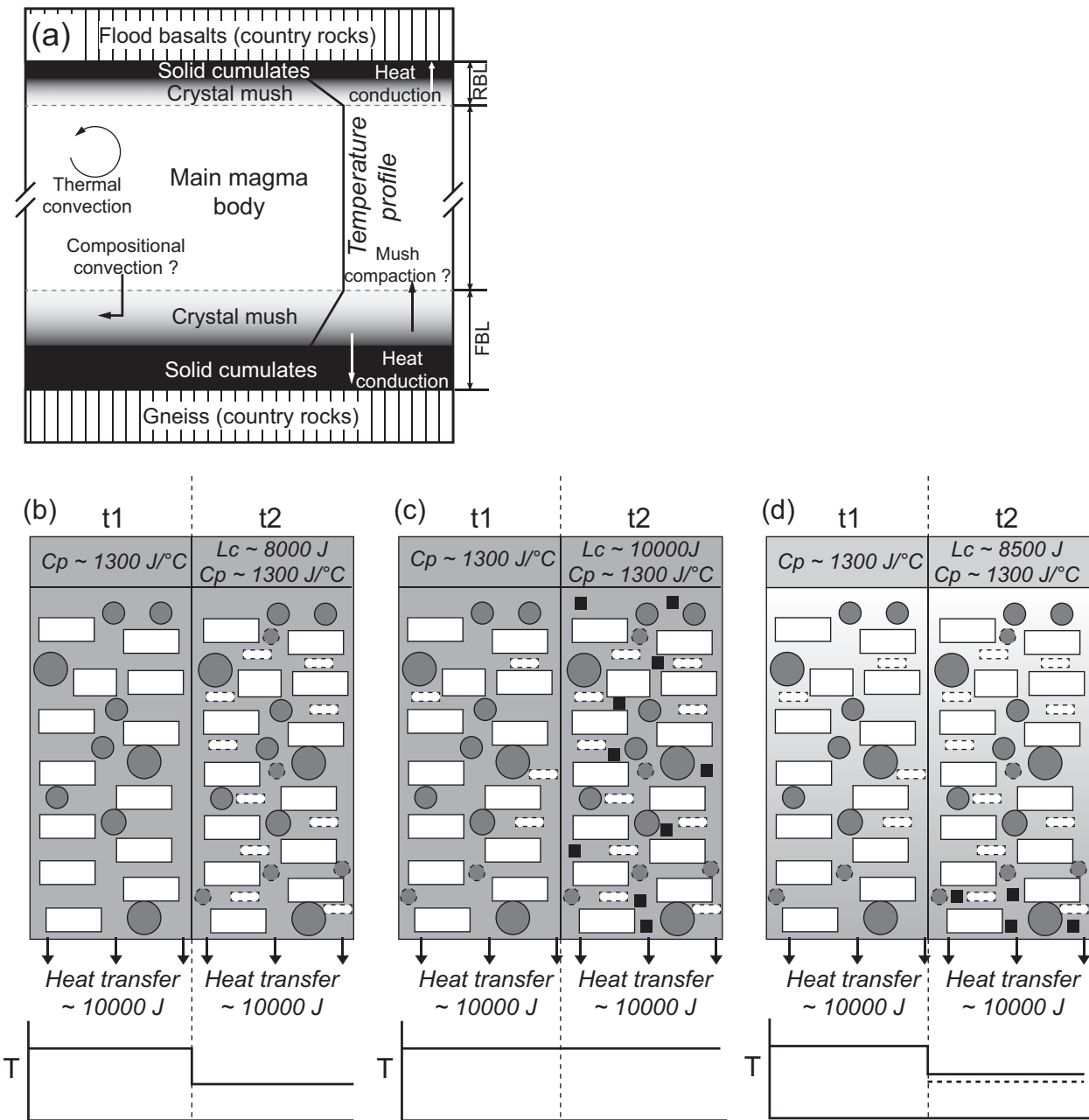
Fig. 20. Effect of liquid fraction on the thermal regime of a crystal mush initially saturated in two phases (plagioclase and olivine) at the appearance of a new interstitial phase (clinopyroxene). (a) Schematic model of a magma chamber developing a crystal mush on the walls [here on the floor and roof of the magma chamber; modified from Kuritani *et al.* (2007)]. The temperature distribution of the melt within the magma chamber is shown for reference. The global system is cooling by heat conduction through the country-rocks. Compaction of the crystal mush and compositional convection may or may not occur, depending on the physical properties of the crystal mush and the stable liquidus assemblage. Thermal convection is thought to occur within the main magma body and could also occur within the crystal mush. FBL, floor boundary layer; RBL, roof boundary layer. (b) Snapshot of the thermal regime of the crystal mush before the crystallization of interstitial phases (t1) and after the crystallization of interstitial phases (t2). The heat lost through the country-rocks needed to cool the system is shown, as is the specific heat of the magma. At t2, the latent heat of crystallization released by the crystallization of the interstitial crystals is not sufficient to thermally buffer the system, which therefore keeps cooling (see the temperature distribution at the bottom of the panel). (c) Thermal effect of the appearance of a new phase. The enhanced release of latent heat at the appearance of the new phase thermally buffers the system and the temperature of the mush liquid at t2 is identical to that at t1. (d) The crystallization of the new interstitial phase occurs at the bottom of the mush and the heat is quickly dissipated to the whole volume of magma (probably as a result of heat advection and heat conduction). The global latent heat of crystallization in the whole volume of magma is not sufficient to keep the system at a constant temperature, but the temperature drop between t1 and t2 might be lower than in (b) (dotted horizontal line).

and observed that the appearance of magnetite occurs at a liquid fraction ranging from $F = 0.92$ (1120°C) to $F = 0.14$ (1065°C; Supplementary Dataset 6). For each composition, our calculations showed an increase in the contribution of latent heat of crystallization to the enthalpy budget at the saturation of magnetite. However, $\Delta H_{fus}/\Delta T$ values per gram of magma are almost identical in all calculations (Supplementary Dataset 6). This suggests that the proportion of liquid in the mush has presumably no influence on the cotectic proportion of any phase and therefore on the thermal regime of the mush liquid, as long as the whole volume of liquid becomes simultaneously saturated in this phase. This indicates that the degree of supersaturation of a mineral component in the melt just before this mineral starts crystallizing is not strongly dependent on the melt fraction (Morse, 1979b). When the new phase saturates, most of the heat extracted is latent heat (Morse, 2011) and the liquid may therefore stay at near-isothermal conditions (compare t2 in Fig. 20b and t2 in Fig. 20c) for tens to thousands of years (Fig. 16) regardless of the interstitial liquid fraction. It is therefore capable of crystallizing plagioclase of constant composition as long as diffusion (see above) can bring the compatible elements towards the crystal–liquid interface.

(2) In a more realistic scenario, the saturation of the new phase does not occur simultaneously everywhere in the mush liquid. Instead, the mush liquid is compositionally and thermally zoned and saturation of the new phase occurs first in the coldest part of the boundary layer. In this case, the enhanced release of latent heat occurs in only the lower part of the mush but the energy released is dissipated in the whole body of the liquid. Depending on the crystal mush thickness (Holness et al., 2007) the extra heat released as the interstitial liquid becomes saturated in a new phase may not be sufficient to maintain an isothermal mush if the rate of heat loss through the intrusion margins exceeds the rate of production of latent heat of crystallization (Fig. 20d).

Dissipating the latent heat within the entire volume of mush liquid requires an efficient process of heat transfer. A high porosity allows heat transfer through thermally induced liquid convection (Brandeis & Marsh, 1990; Worster, 1991), whereas a low porosity allows heat transfer only through diffusion. In a plutonic setting it has been shown that temperature buffering owing to latent heat release at the eutectic point is c. 1000 times faster at high porosity ($>40\%$) than at low porosity (Huber et al., 2009), presumably because of the relatively low heat diffusivity in both crystals (10^{-6}–$10^{-7}\,m^2\,s^{-1}$; Xu et al., 2004; Branlund & Hofmeister, 2012; Hofmeister, 2012) and liquid ($10^{-7}\,m^2\,s^{-1}$; Huppert & Sparks, 1988). Other experiments

have shown that the transition between conduction-dominated and advection-dominated heat transfer occurs at porosities of 10–15% (Lima et al., 2005). This is consistent with numerical simulations by Cheadle et al. (2004) showing that the permeability of a crystal mush significantly drops when the porosity is reduced below 15–20%. We suggest that efficient thermal and compositional buffering of the mush liquid is most likely to be effective when the mush porosity is lower than 15–20%. At higher porosity, the latent heat is dissipated to the whole volume of mush liquid too quickly to have a significant effect on its cooling rate (e.g. the global latent hear cannot counteract the heat lost though the walls) and therefore on equilibrium plagioclase composition.

Heterogeneous porosity distribution in the Skaergaard mush

In the previous section, we have suggested that whether or not plagioclase grains develop a rim of constant composition at the appearance of a new phase mainly depends on the porosity of the crystal mush when this phase appears. Our sample set includes those dominated by grains with buffered rims (Type I), whereas others are dominated by grains with normal zoning (Type II) or unzoned grains (Type III). This indicates that the porosity distribution was probably heterogeneous in the Skaergaard crystal mush during solidification. Heterogeneous porosity within the crystal mush could partly result from a change of the crystal mush thickness with differentiation (e.g. Holness et al., 2007, 2009b; Holness, 2012; Namur et al., 2013) or from contrasted crystal mush thicknesses in the various series (LS, MBS and UBS) of the intrusion. Changing the crystal mush thickness would, in order to have an effect, have to change the volume of liquid affected by the saturation of a new interstitial phase (Fig. 20), and therefore the thermal history of the crystal mush. Below, we discuss the porosity conditions under which the three types of plagioclase grains may have formed.

Compositionally buffered (Type I) grains

Type I grains must develop in a crystal mush with sufficient porosity to allow the crystallization of large (up to 800 μm) rims of constant composition at the saturation of a new cumulus phase (Fig. 21a; grain 1). However, as discussed above, the porosity cannot be much higher than 15–20% because a very large, interconnected, porosity would allow efficient thermal advection within the crystal mush and would therefore annihilate any thermal effect associated with the saturation of a new phase in the mush liquid. Type I plagioclase grains are especially abundant in the lower part of the LS (LZa–LZb). The proportion of solidified interstitial melt in these rocks is in the range 20–40%, which we can consider as a first-order estimate of the initial porosity (Fig. 19). This value is lower than porosity estimates based on numerical simulation (e.g. 60%;
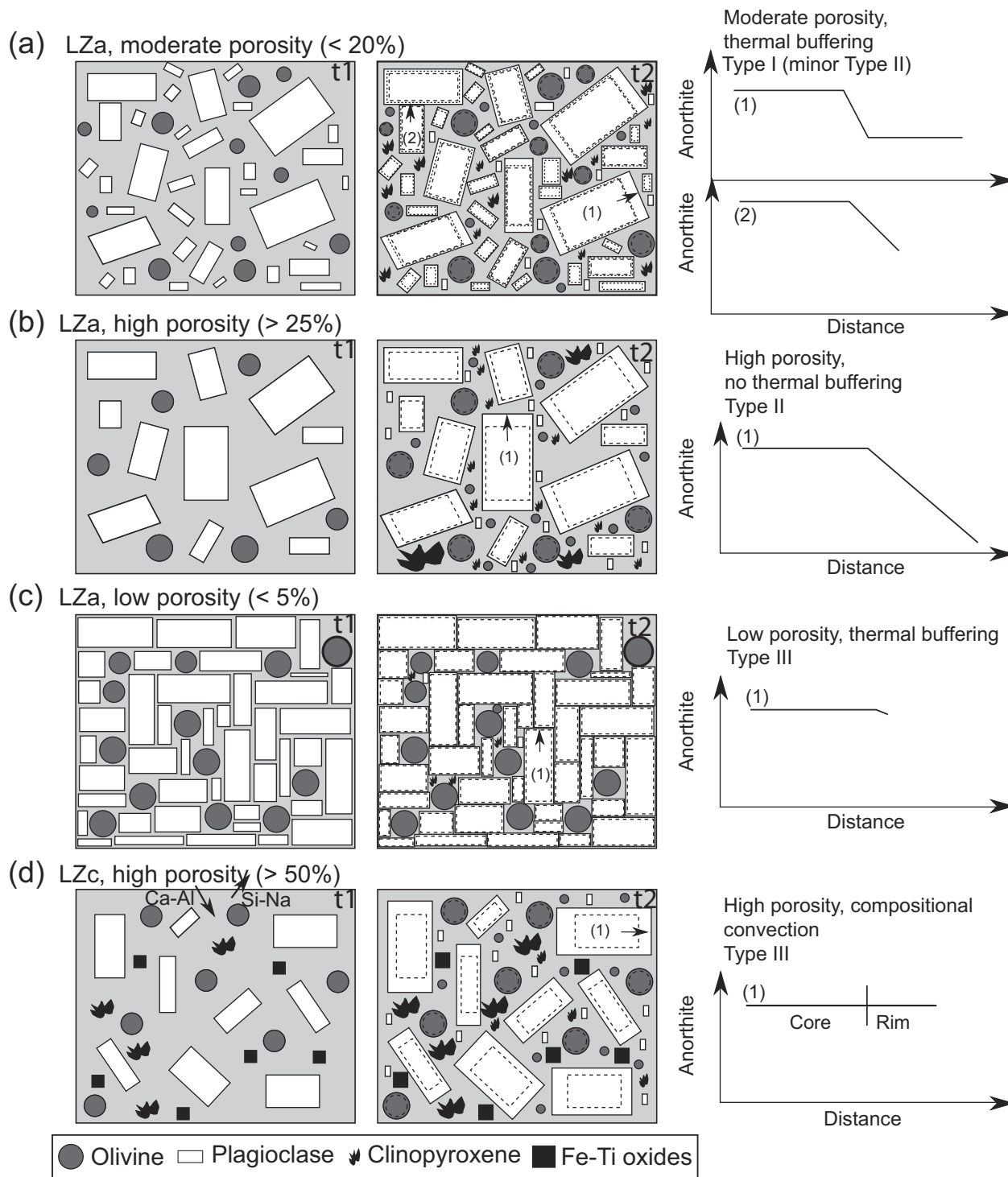
Fig. 21. Schematic representation of a Skaergaard crystal mush and the effect of the liquid fraction on plagioclase compositional profiles. This series of diagrams shows a snapshot of a subsection (lowest and coldest, part) of the mush before (t1) the saturation of a new phase (clinopyroxene or Fe–Ti oxides) and after (t2) the saturation of the new phase. (a) LZa (plagioclase–olivine + interstitial clinopyroxene) crystal mush with moderate porosity. Saturation of interstitial clinopyroxene results in efficient thermal buffering of the mush liquid. Plagioclase grains surrounded by liquid will develop a thin mantle of decreasing An content and large rims of constant composition (see grain 1). Grains in contact cannot grow further and do not develop these rims (they may or may not develop a mantle; see grain 2). The dashed line represents the limit between the core and the mantle of decreasing An content, whereas the dotted line represents the limit between the mantle and the rim of constant composition. (b) LZa crystal mush with high porosity (>30%). Owing to heat advection, the saturation of interstitial clinopyroxene does not

(continued)

Jerram *et al.*, 2003), indicating that the lower zone of the LS may have been rapidly compacted during solidification (Tegner *et al.*, 2009). Saturation of clinopyroxene and Fe–Ti oxides occurs when the proportion of residual melt (F) in the magma chamber is *c.* 0·7 and 0·5 respectively (Nielsen, 2004). Considering that interstitial phases saturate in the mush liquid at a stage of liquid evolution similar to that at the appearance of cumulus phases in the main magma body (Humphreys, 2009), we can calculate that the porosity was in the range 12–24 vol. % at the saturation of interstitial clinopyroxene and 10–20 vol. % at the saturation of interstitial magnetite. These values indicate that Type I grains in LZa–LZb samples probably formed in a mush with a porosity close to the maximum value at which Type I grains are likely to form.

Normally zoned (Type II) plagioclase grains

Type II plagioclase grains are generally a minor component in rocks dominated by Type I grains (e.g. in LZa–LZb) but form a major component in the upper part of the LS (UZb), in the MBS and in UBS.

Where associated with Type I plagioclase grains (e.g. in LZa–LZb), the most evolved composition of the rims of Type II grains is often identical to the composition of buffered rims in Type I grains. There is, however, some variability and grains with more An-rich rims also occur. The absence of rims of constant composition on some grains is most likely to result from impingement of adjacent grains before the process of latent heat buffering actually starts (Fig. 2la; grain 2).

Where Type II plagioclase grains dominate the plagioclase population (i.e. UZb, MBS, UBS), the rims have a compositional range locally exceeding 40% An and approach a pure albite endmember in some samples. We suggest that efficient latent heat buffering did not occur (or did not last for a long period of time) in most parts of the MBS and UBS crystal mush because of the large fraction of interstitial melt. For the non-compacting MBS and UBS, assuming an initial porosity of 0·6, we calculate that clinopyroxene and Fe–Ti oxides will appear in the lowest stratigraphic part of the MBS and UBS when the mush liquid fraction is higher than 25–40 vol. %. This relatively high porosity is likely to have resulted in efficient thermal advection, hampering any latent heat buffering in this part of the mush (Huber *et al.*, 2009). The rims of Type II

grains were thus presumably formed by simple crystallization from a continuously evolving melt, with no extensive period of plagioclase growth at constant composition (Fig. 2lb). Plagioclase rims with the most evolved compositions might also have been produced by the crystallization of a late-stage Si-rich immiscible melt (Humphreys, 2011).

Unzoned (Type III) plagioclase grains

Unzoned grains are the dominant type of grains in LZc and are very common from MZ to the top of the LS. The presence of unzoned grains may imply that after the initial stage of crystal core formation at the magma–mush interface, consequent progressive burial of the crystals was associated with a very low fraction of interstitial liquid, perhaps as a consequence of gravitationally driven compaction (Fig. 2lc; Tegner *et al.*, 2009; McKenzie, 2011). Alternatively, the absence of zoning might point to effective compositional convection in the interstitial liquid (Fig. 2ld; Toplis *et al.*, 2008). In any case, the presence of abundant Type III grains in Skaergaard confirms that the mush liquid was mobile, at least locally. Unzoned (Type III) grains are closely associated with zoned grains (Type I or Type II) in many samples of the Skaergaard, and especially from MZ to UZb of the LS. This suggests that the mush porosity may have been heterogeneous even at a millimetre to centimetre scale (or even less). As suggested by Toplis *et al.* (2008), this may indicate that compositional convection (or compaction) is not an efficient mechanism for expelling or exchanging the interstitial melt.

CONCLUSIONS

Our examination of plagioclase from the Layered Series, Marginal Series and Upper Border Series of the Skaergaard intrusion allows us to identify three types of compositional profile, as follows.

(1) Type I grains with a core of constant An content, surrounded by a mantle of decreasing An and a rim of constant An content. These are especially common in the Layered Series. Only three compositions of rims are observed (An_{56}, An_{51} and An_{41}), each of them having a well-defined stratigraphic distribution.
(2) Type II grains with a core of constant composition and a rim of decreasing An.
(3) Unzoned Type III plagioclase grains.

Fig. 21 Continued

provide sufficient release of latent heat to thermally buffer the mush liquid (see Fig. 20d). Plagioclase rims will develop normal zoning. The dashed line represents the boundary between the core and the rim of decreasing An content. (c) LZa crystal mush with very low porosity. Saturation of clinopyroxene results in efficient thermal buffering but the porosity is almost closed when clinopyroxene appears. Plagioclase grains cannot grow further and are mostly unzoned (they develop only a very thin rim of decreasing An content; dashed line). (d) LZc (plagioclase–olivine–clinopyroxene–Fe–Ti oxides) crystal mush with convective exchange between the mush liquid and the main magma body (not represented). Convective exchange brings compatible elements to the crystallization sites and removes incompatible elements, resulting in the crystallization of unzoned plagioclase. The dashed line represent the limit between the core, which crystallized at the top of the mush, and the rim, which crystallized in the crystal mush (see text for details). It should be noted that core and rim have the same composition.

Type III grains can be related either to a low fraction of interstitial melt (Tegner *et al.*, 2009) or to compositional convection within the mush (Toplis *et al.*, 2008), whereas Type II grains with normal zoning can be interpreted as a consequence of *in situ* crystallization during simple differentiation. In contrast, Type I grains cannot be explained by these processes.

Mobility of the interstitial liquid owing to either compaction of the crystal mush (Tegner *et al.*, 2009; McKenzie, 2011) or gravitationally driven phase separation of immiscible liquids (Holness *et al.*, 2011; Humphreys, 2011) cannot be responsible for the formation of Type I plagioclase grains in Skaergaard. They also cannot be accounted for by either selective mineral dissolution in the crystal mush (Higgins, 1998) or grain boundary reorganization (Svahnberg & Piazolo, 2013). Compositional convection within the crystal mush may have contributed to some extent to the formation of constant composition rims, but this process alone cannot explain all the compositional features that we see in Type I grains and their presence in all three series of the Skaergaard intrusion. Instead, we suggest that the rims were buffered to a constant composition as a result of extended periods of near-isothermal adcumulus crystallization.

Saturation of the mush liquid in a new phase results in a temporary overproduction of this phase. During this period of overproduction, the release of latent heat of crystallization is sufficiently high to keep the mush liquid at its liquidus temperature for a period of time that may range from tens to thousands of years. Diffusion of chemical species in the melt towards and away from the melt–crystal interface is likely to be sufficiently rapid to maintain the liquid at a constant composition. Adcumulus crystallization of plagioclase under these conditions can account for the formation of the large rims of constant composition that distinguish Type I grains. This also explains why only three rim compositions are observed ($An_{56\pm2}$, $An_{51\pm1}$ and $An_{41\pm1}$)—these compositions correspond the An content of plagioclase primocrysts at the first appearance of clinopyroxene, Fe–Ti oxides and apatite, respectively.

The porosity of the crystal mush at the point of saturation of the new phase exerts a primary control on the efficiency of the latent heat buffering process. Where the porosity is sufficiently high to permit efficient heat advection (e.g. >15–20 vol. %), the extra latent heat liberated is quickly dissipated. As a consequence, the global latent heat of crystallization cannot counterbalance the heat lost through the walls of the magma chamber and the crystal mush keeps cooling. Crystallization in this context results in the formation of plagioclase overgrowths with normal zoning (Type II grains).

The presence of various types of plagioclase grains in Skaergaard indicates that the porosity of the crystal mush was highly heterogeneous not only on large length scales but also on the scale of a single thin section. The presence of unzoned Type III grains confirms that the mush liquid was, at least locally, highly mobile during the crystal mush solidification process.

SUPPLEMENTARY DATA

Supplementary data for this paper are available at *Journal of Petrology* online.

REFERENCES

Albarède, F. & Bottinga, Y. (1972). Kinetic disequilibrium in trace element partitioning between phenocrysts and host lava. *Geochimica et Cosmochimica Acta* **36**, 141–156.

Andrews, G. D., Branney, M. J., Bonnichsen, B. & McCurry, M. (2008). Rhyolitic ignimbrites in the Rogerson Graben, southern Snake River Plain volcanic province: Volcanic stratigraphy, eruption history and basin evolution. *Bulletin of Volcanology* **70**, 269–291.

Bindeman, I. N. & Davis, A. M. (1999). Convection and redistribution of alkalis and trace elements during the mingling of basaltic and rhyolite melts. *Petrology* **7**, 91–101.

Boorman, S., Boudreau, A. & Kruger, F. J. (2004). The Lower Zone–Critical Zone transition of the Bushveld Complex: a quantitative textural study. *Journal of Petrology* **45**, 1209–1235.

Brandeis, G. & Jaupart, C. (1986). On the interaction between convection and crystallization in cooling magma chambers. *Earth and Planetary Science Letters* **77**, 345–361.

Brandeis, G. & Marsh, B. D. (1990). Transient magmatic convection prolonged by solidification. *Geophysical Research Letters* **17**, 1125–1128.

Brandeis, G., Jaupart, C. & Allègre, C. (1984). Nucleation, crystal growth and the thermal regime of cooling magmas. *Journal of Geophysical Research* **89**, 10161–10177.

Branlund, J. M. & Hofmeister, A. M. (2012). Heat transfer in plagioclase feldspars. *American Mineralogist* **97**, 1145–1154.

Byerly, G. R., Melson, W. G. & Vogt, P. R. (1976). Rhydacites, andesites, ferro-basalts and ocean tholeiites from the Galapagos Spreading Centre. *Earth and Planetary Science Letters* **30**, 215–221.

Cabane, H., Laporte, D. & Provost, A. (2005). An experimental study of Ostwald Ripening of olivine and plagioclase in silicate melts: implications for the growth and size of crystals in magmas. *Contributions to Mineralogy and Petrology* **150**, 37–53.

Carmichael, I. S. (1964). The petrology of the Thingmuli, a Tertiary volcano in eastern Iceland. *Journal of Petrology* **5**, 435–460.

Cashman, K. V. (1993). Relationship between plagioclase crystallization and cooling rate in basaltic melts. *Contributions to Mineralogy and Petrology* **113**, 126–142.

Charlier, B. & Grove, T. L. (2012). Experiments on liquid immiscibility along tholeiitic liquid lines of descent. *Contributions to Mineralogy and Petrology* **164**, 27–44.

Chaudhuri, P. & Marron, J. S. (1999). SiZer for exploration of structure in curves. *Journal of the American Statistical Association* **94**, 807–823.

Cheadle, M. J., Elliott, M. T. & McKenzie, D. (2004). Percolation threshold and permeability of crystallizing igneous rocks: The importance of textural equilibrium. *Geology* **32**, 757–760.

Chistyakova, S. & Latypov, R. (2012). Magma differentiation and crystallization in basaltic conduits by two competing petrogenetic processes. *Lithos* **148**, 142–161.

Costa, F., Coogan, L. A. & Chakraborty, S. (2012). The time scales of magma mixing and mingling involving primitive melts and melt–mush interaction at mid-ocean ridges. *Contributions to Mineralogy and Petrology* **159**, 371–387.

Couch, S., Harford, C. L., Sparks, R. S. J. & Carroll, M. R. (2003). Experimental constraints on the conditions of formation of highly calcic plagioclase microlites at the Soufrière Hills volcano, Monserrat. *Journal of Petrology* **44**, 1455–1475.

Dunbar, N. W., Jacobs, G. K. & Naney, M. T. (1995). Crystallisation processes in an artificial magma: variations in crystal shape, growth rate and composition with melt cooling history. *Contributions to Mineralogy and Petrology* **120**, 412–425.

Duong, T., Cowling, A., Koch, I. & Wand, M. (2008). Feature significance for multivariate kernel density estimation. *Computational Statistics and Data Analysis* **52**, 4225–4242.

Fraley, C. & Raftery, A. E. (2002). Model-based clustering, discriminant analysis, and density estimation. *Journal of the American Statistical Association* **978**, 611–631.

Ghiorso, M. S. (1991). Temperatures in and around cooling magma bodies. In: Perchuk, L. L. (ed.) *Progress in Metamorphic and Magmatic Petrology.* Cambridge University Press, pp. 387–410.

Ghiorso, M. S. (1997). Thermodynamic models of igneous processes. *Annual Review of Earth and Planetary Sciences* **25**, 221–241.

Ghiorso, M. S. & Carmichael, I. S. E. (1985). Chemical mass transfer in magmatic processes. II. Applications in equilibrium crystallization, fractionation and assimilation. *Contributions to Mineralogy and Petrology* **90**, 121–141.

Ghiorso, M. S. & Sack, R. O. (1995). Chemical mass transfer in magmatic processes IV. A revised model and internally consistent thermodynamic model for the interpolation and extrapolation of liquid–solid equilibria in magmatic systems at elevated temperatures and pressures. *Contributions to Mineralogy and Petrology* **119**, 197–212.

Giletti, B. J. & Shanahan, T. M. (1997). Alkali diffusion in plagioclase feldspar. *Chemical Geology* **139**, 3–20.

Grove, T. L., Baker, M. B. & Kinzler, R. J. (1984). Coupled CaAl–NaSi diffusion in plagioclase feldspar: Experiments and application to cooling rate speedometry. *Geochimica et Cosmochimica Acta* **48**, 2113–2121.

Hansen, H. & Gronvold, K. (2000). Plagioclase ultraphyric basalts in Iceland: the mush of the rift. *Journal of Volcanology and Geothermal Research* **98**, 1–32.

Higgins, M. D. (1998). Origin of anorthosite by textural coarsening: quantitative measurements of a natural sequence of textural development. *Journal of Petrology* **39**, 1307–1323.

Higgins, M. D. (2002). The role of textural coarsening in the development of the Kiglapait layered mafic intrusion, Labrador, Canada: a crystal size distribution study. *Contributions to Mineralogy and Petrology* **144**, 314–330.

Hofmeister, A. M. (2012). Thermal diffusivity of orthopyroxenes and protoenstatite as a function of temperature and chemical composition. *European Journal of Mineralogy* **24**, 669–681.

Holness, M. B. (2012). The thickness of crystal mushy layers on magma chamber floors. *Geophysical Research Abstracts* **14**, 2340.

Holness, M. B., Tegner, C., Nielsen, T. F., Stripp, G. & Morse, S. A. (2007). A textural record of solidification and cooling in the Skaergaard intrusion, East Greenland. *Journal of Petrology* **48**, 2359–2377.

Holness, M. B., Morse, S. A. & Tegner, C. (2009a). Response to comment by McBirney, Boudreau and Marsh. *Journal of Petrology* **50**, 97–102.

Holness, M. B., Tegner, C. & Nielsen, T. F. (2009b). Constraining the thickness of the crystal mush in layered mafic intrusions. American Geophysical Union Fall Meeting, San Francisco, V13F-05 Eos, Transactions, American Geophysical Union 90.52.

Holness, M. B., Stripp, G., Humphreys, M. C. S., Veksler, I. V., Nielsen, T. F. D. & Tegner, C. (2011). Silicate liquid immiscibility within the crystal mush: Late-stage magmatic microstructures in the Skaergaard intrusion, East Greenland. *Journal of Petrology* **52**, 175–222.

Holness, M. B., Namur, O. & Cawthorn, R. G. (2013). Disequilibrium dihedral angles in layered intrusions: the microstructural record of fractionation. *Journal of Petrology* **54**, 2067–2093.

Hoover, J. D. (1989a). Petrology of the Marginal Border Series of the Skaergaard intrusion. *Journal of Petrology* **30**, 399–439.

Hoover, J. D. (1989b). The chilled marginal gabbro and other contact rocks of the Skaergaard intrusion. *Journal of Petrology* **30**, 441–476.

Hort, M. & Spohn, T. (1991a). Numerical simulation of the crystallization of multicomponent melts in thin dikes or sills 2. Effects of heterocatalytic nucleation and composition. *Journal of Geophysical Research* **96**, 485–499.

Hort, M. & Spohn, T. (1991b). Crystallization calculations for a binary melt cooling at constant rates of heat removal: implications for the crystallization of magma bodies. *Earth and Planetary Science Letters* **107**, 463–474.

Huber, C., Bachmann, O. & Manga, M. (2009). Homogenization processes in silicic magma chambers by stirring and mushification (latent heat buffering). *Earth and Planetary Science Letters* **283**, 38–47.

Humphreys, M. C. S. (2009). Chemical evolution of intercumulus liquid, as recorded in plagioclase overgrowth rims from the Skaergaard intrusion. *Journal of Petrology* **50**, 127–145.

Humphreys, M. C. S. (2011). Silicate liquid immiscibility within the crystal mush: Evidence from Ti in plagioclase from the Skaergaard intrusion. *Journal of Petrology* **52**, 147–174.

Hunter, R. H. & Sparks, R. S. (1987). The differentiation of the Skaergaard intrusion. *Contributions to Mineralogy and Petrology* **95**, 451–461.

Huppert, E. H. & Sparks, R. S. (1988). The generation of granitic magmas by intrusion of basalt into continental crust. *Journal of Petrology* **29**, 599–624.

Irvine, T. N. (1980). Magmatic infiltration metasomatism, double-diffusive fractional crystallization, and adcumulus growth in the Muskox intrusion and other layered intrusions. In: Hargrave, R. B. (ed.) *Physics of Magmatic Processes*. Princeton University Press, pp. 325–383.

Jang, Y. D. & Naslund, H. R. (2001). Major and trace element composition of Skaergaard plagioclase, geochemical evidence for changes in magma dynamics during the final stage of crystallization of the Skaergaard intrusion. *Contributions to Mineralogy and Petrology* **140**, 441–457.

Jerram, D. A., Cheadle, M. J. & Philpotts, A. R. (2003). Quantifying the building blocks of igneous rocks: Are clustered crystal frameworks the foundation? *Journal of Petrology* **44**, 2033–2051.

Kerr, R. C. & Tait, S. R. (1986). Crystallization and compositional convection in a porous medium with application to layered igneous intrusions. *Journal of Geophysical Research* **91**, 3591–3608.

Kamenetsky, V. S., Everard, J. L., Crawford, A. J., Varne, R., Eggins, S. M. & Lanyon, R. (2000). Enriched end-member or primitive MORB melts: Petrology and geochemistry of glasses from Macquarie Island (SW Pacific). *Journal of Petrology* **41**, 411–430.

Kuritani, T., Yokoyama, T. & Nakamura, E. (2007). Rates of thermal and chemical evolution of magmas in a cooling magma chamber: a chronological and theoretical study on basaltic and andesitic lavas from Rishiri Volcano, Japan. *Journal of Petrology* **48**, 1295–1319.

Lange, R. A., Cashman, K. V. & Navrotsky, A. (1994). Direct measurements of latent heat during crystallization and melting of a ugandite and an olivine basalt. *Contributions to Mineralogy and Petrology* **118**, 169–181.

Larsen, R. B. & Tegner, C. (2006). Pressure conditions for the solidification of the Skaergaard intrusion: eruption of East Greenland flood basalts in less than 300,000 years. *Lithos* **92**, 181–197.

Lifshitz, I. M. & Slyozov, V. V. (1961). The kinetics of precipitation from supersaturated solid solutions. *Journal of Physics and Chemistry of Solids* **19**, 35–50.

Lima, W. M., Biondo, V., Weinand, W. R., Nogueira, E. S., Medina, A. N., Baesso, M. L. & Bento, A. C. (2005). The effect of porosity on thermal properties: Towards a threshold of particle contact in sintered stainless steel. *Journal of Physics—Condensed Matter* **17**, 1239–1249.

Longhi, J., Vander Auwera, J., Fram, M. S. & Monthieth, J. N. (1993). Pressure effects, kinetics and rheology of anorthositic and related magmas. *American Mineralogist* **78**, 1016–1030.

Loomis, T. P. (1982). Numerical simulations of crystallization processes of plagioclase in complex melts: the origin of major and oscillatory zoning in plagioclase. *Contributions to Mineralogy and Petrology* **81**, 219–229.

Maaloe, S. (1976). The zoned plagioclase of the Skaergaard intrusion, East Greenland. *Journal of Petrology* **17**, 318–419.

McBirney, A. R. (1989). The Skaergaard layered series: I. Structure and average compositions. *Journal of Petrology* **30**, 363–397.

McBirney, A. R. & Hunter, R. H. (1995). The cumulate paradigm reconsidered. *Journal of Geology* **103**, 114–122.

McBirney, A. R. & Naslund, H. R. (1990). The Differentiation of the Skaergaard intrusion. A discussion of Hunter & Sparks. *Contributions to Mineralogy and Petrology* **104**, 235–247.

McBirney, A. R. & Noyes, R. M. (1979). Crystallization and layering of the Skaergaard intrusion. *Journal of Petrology* **20**, 487–554.

McKenzie, D. P. (1984). The generation of compaction of partially molten rock. *Journal of Petrology* **25**, 713–765.

McKenzie, D. (2011). Compaction and crystallization in magma chambers: towards a model of the Skaergaard intrusion. *Journal of Petrology* **52**, 905–930.

Means, W. D. & Park, Y. (1994). New experimental approach to understanding igneous texture. *Geology* **22**, 323–326.

Meurer, W. D. & Boudreau, A. E. (1996). Petrology and mineral compositions of the Middle Banded Series of the Stillwater Complex, Montana. *Journal of Petrology* **37**, 583–607.

Meurer, W. P. & Claeson, D. T. (2002). Evolution of crystallizing interstitial liquid in an arc-related cumulate determined by LA ICP-MS mapping of a large amphibole oikocryst. *Journal of Petrology* **43**, 607–629.

Mills, R. D. & Glazner, A. F. (2013). Experimental study on the effects of temperature cycling on coarsening of plagioclase and olivine in an alkali basalt. *Contributions to Mineralogy and Petrology* **166**, 97–111.

Mills, R. D., Ratner, J. J. & Glazner, A. F. (2011). Experimental evidence for crystal coarsening and fabric development during temperature cycling. *Geology* **39**, 1139–1142.

Morse, S. A. (1979*a*). Kiglapait geochemistry I: Systematics, sampling and density. *Journal of Petrology* **20**, 555–590.

Morse, S. A. (1979*b*). Kiglapait geochemistry II: Petrography. *Journal of Petrology* **20**, 591–624.

Morse, S. A. (1986). Convection in aid of adcumulus growth. *Journal of Petrology* **27**, 1183–1214.

Morse, S. A. (2008*a*). Compositional convection trumps silicate liquid immiscibility in layered intrusions: a discussion of 'Liquid immiscibility and the evolution of basaltic magma' by Veksler *et al.*, *Journal of Petrology* 48, 2187–2210. *Journal of Petrology* **49**, 2157–2168.

Morse, S. A. (2008*b*). Toward a thermal model for the Skaergaard liquidus. *American Mineralogist* **93**, 248–251.

Morse, S. A. (2011). The fractional latent heat of crystallizing magmas. *American Mineralogist* **96**, 682–689.

Morse, S. A. (2012). Plagioclase An range and residual porosity in igneous cumulates of the Kiglapait intrusion. *Journal of Petrology* **53**, 891–918.

Muncill, G. E. & Lasaga, A. C. (1987). Crystal-growth kinetics of plagioclase in igneous systems: one-atmosphere experiments and application of a simplified growth model. *American Mineralogist* **72**, 299–311.

Namur, O. & Charlier, B. (2012). Efficiency of compaction and compositional convection during mafic crystal mush solidification: the Sept Iles layered intrusion, Canada. *Contributions to Mineralogy and Petrology* **163**, 1049–1068.

Namur, O., Charlier, B., Toplis, M. J., Higgins, M. D., Liégeois, J. P. & Vander Auwera, J. (2010). Crystallization sequence and magma chamber processes in the ferrobasaltic Sept Iles layered intrusion, Canada. *Journal of Petrology* **51**, 1203–1236.

Namur, O., Charlier, B., Toplis, M. J. & Vander Auwera, J. (2012). Prediction of plagioclase–melt equilibria in anhydrous silicate melts at 1-atm. *Contributions to Mineralogy and Petrology* **163**, 133–150.

Namur, O., Humphreys, M. C. S. & Holness, M. B. (2013). Lateral reactive infiltration in a vertical gabbroic crystal mush, Skaergaard intrusion, East Greenland. *Journal of Petrology* **54**, 985–1016.

Naslund, H. R. (1984). Petrology if the Upper Border Series of the Skaergaard intrusion. *Journal of Petrology* **25**, 185–212.

Nielsen, T. F. D. (2004). The shape and volume of the Skaergaard intrusion, Greenland: Implications for mass balance and bulk composition. *Journal of Petrology* **45**, 507–530.

Panjasawatwong, Y., Danyushevsky, L., Crawford, A. J. & Harris, K. L. (1995). An experimental study of the effects of melt composition on plagioclase–melt equilibria at 5 and 10 kbar: Implications for the origin of magmatic high-An plagioclase. *Contributions to Mineralogy and Petrology* **118**, 420–432.

Philpotts, A. R., Shi, J. & Brutsman, C. (1998). Role of plagioclase crystal chains in the differentiation of partly crystallized basaltic magma. *Nature* **395**, 343–346.

Pupier, E., Duchene, S. & Toplis, M. J. (2008). Experimental quantification of plagioclase crystal size distribution during cooling of a basaltic liquid. *Contributions to Mineralogy and Petrology* **155**, 555–570.

Putirka, K. D. (2005). Igneous thermometers and barometers based on plagioclase + liquid equilibria: Tests of some existing models and new calibrations. *American Mineralogist* **90**, 336–346.

Rudge, J. (2008). Finding peaks in geochemical distributions: a re-examination of the helium–continental crust correlation. *Earth and Planetary Science Letters* **274**, 179–188.

Salmonsen, L. P. & Tegner, C. (2013). Crystallization sequence of the Upper Border Series of the Skaergaard intrusion: Revised subdivision and implications for chamber-scale magma homogeneity. *Contributions to Mineralogy and Petrology* **165**, 1155–1171.

Schiavi, F., Walte, N. & Keppler, H. (2009). First *in situ* observation of crystallization processes in basaltic–andesitic melt with the moissanite cell. *Geology* **37**, 963–966.

Schmidt, M. W., Forien, M., Solferino, G. & Bagdassarov, N. (2012). Settling and compaction of olivine in basaltic magmas: an experimental study on the time scales of cumulate formation. *Contributions to Mineralogy and Petrology* **164**, 959–976.

Settle, M. (1979). Lava rheology: Thermal buffering produced by the latent heat of crystallization, *Proceedings of the 10th Lunar and Planetary Science Conference. Geochimica et Cosmochimica Acta Supplement* 1107–1109.

Sheather, S. J. & Jones, M. C. (1991). A reliable data-based bandwidth selection method for kernel density estimation. *Journal of the Royal Statistical Society, Series B* **53**, 683–690.

Shirley, N. D. (1986). Compaction of igneous cumulates. *Journal of Geology* **94**, 795–809.

Silverman, B. W. (1986). *Density Estimation for Statistics and Data Analysis. Monographs on Statistics and Applied Probability.* Chapman & Hall, 22 pp.

Simakin, A. G. & Bindeman, L. N. (2008). Evolution of crystal sizes in the series of dissolution and precipitation events in open magma systems. *Journal of Volcanology and Geothermal Research* **177**, 997–1010.

Smith, P. & Asimow, P. D. (2005). Adiabat_1ph: A new public front-end to the MELTS, pMELTS, and pHMELTS models. *Geochemistry, Geophysics, Geosystems* **6**, Q02004, doi:10.1029/2004GC000816.

Spera, F. J. & Bohrson, W. A. (2001). Energy-constrained open-system magmatic processes I: General model and energy-constrained assimilation and fractional crystallization (EC-AFC) formulation. *Journal of Petrology* **42**, 999–1018.

Svahnberg, H. & Piazolo, S. (2013). Interaction of chemical and physical processes during deformation at fluid-present conditions: a case study from an anorthosite–leucogabbro deformed at amphibolite facies conditions. *Contributions to Mineralogy and Petrology* **165**, 543–562.

Tait, S. R., Huppert, H. E. & Sparks, R.S. (1984). The role of compositional convection in the formation of adcumulate rocks. *Lithos* **17**, 139–146.

Tegner, C. (1997). Iron in plagioclase as a monitor of the differentiation of the Skaergaard intrusion. *Contributions to Mineralogy and Petrology* **128**, 45–51.

Tegner, C. & Cawthorn, R. G. (2010). Iron in plagioclase in the Bushveld and Skaergaard intrusions: Implications for iron contents in evolving basic magmas. *Contributions to Mineralogy and Petrology* **159**, 719–730.

Tegner, C., Thy, P., Holness, M. B., Jakobsen, J. K. & Lesher, C. E. (2009). Differentiation and compaction in the Skaergaard intrusion. *Journal of Petrology* **50**, 813–840.

Tegner, C., Lesher, C. E., Holness, M. B., Jakobsen, J. K., Salmonsen, L. P., Humphreys, M. C. S. & Thy, P. (2011). Efficiency of differentiation in the Skaergaard magma chamber, 2011 Fall Meeting, American Geophysical Union, San Francisco, California, 5–9 December, Abstract V33F-06.

Thompson, A. & Maclennan, J. (2013). The distribution of olivine composition in Icelandic basalts and picrites. *Journal of Petrology* **54**, 745–768.

Thy, P., Lesher, C. E. & Tegner, C. (2009*a*). The Skaergaard liquid line of descent revisited. *Contributions to Mineralogy and Petrology* **157**, 735–747.

Thy, P., Tegner, C. & Lesher, C. E. (2009*b*). Liquidus temperatures of the Skaergaard magma. *American Mineralogist* **94**, 1371–1376.

Thy, P., Lesher, C. E., Nielsen, T. F. D. & Brooks, C. K. (2006). Experimental constraints on the Skaergaard liquid line of descent. *Lithos* **92**, 154–180.

Toplis, M. J. & Carroll, M. R. (1995). An experimental study of the influence of oxygen fugacity on Fe-Ti oxide stability, phase relations, and mineral-melt equilibria in ferro-basaltic systems. *Journal of Petrology* **36**, 1137–1170.

Toplis, M. J. & Carroll, M. R. (1996). Differentiation of ferro-basaltic magmas under conditions open and closed to oxygen: implications for the Skaergaard intrusion and other natural systems. *Journal of Petrology* **37**, 837–858.

Toplis, M. J., Brown, W. L. & Pupier, E. (2008). Plagioclase in the Skaergaard intrusion. Part 1: Core and rim compositions in the Layered Series. *Contributions to Mineralogy and Petrology* **155**, 329–340.

Wager, L. R. & Brown, G. M. (1968). *Layered Igneous Rocks*. Oliver & Boyd.

Wager, L. R. & Deer, W. A. (1939). Geological investigations in east Greenland. Part III. The petrology of the Skaergaard intrusion, Kangerdlugssuaq, East Greenland. *Meddelelser om Gronland* **105**, 352.

Wager, L. R., Brown, G. M. & Wadsworth, W. J. (1960). Types of igneous cumulates. *Journal of Petrology* **1**, 73–85.

Wiebe, R. A. & Snyder, D. (1993). Slow, dense replenishments of a basic magma chamber: the layered series of the Newark Island layered intrusion, Nain, Labrador. *Contributions to Mineralogy and Petrology* **113**, 59–72.

Worster, M. G. (1991). Natural convection in a mushy layer. *Journal of Fluid Mechanics* **224**, 335–359.

Worster, M. G. (1997). Convection in mushy layers. *Annual Review of Fluid Mechanics* **29**, 91–122.

Worster, M. G., Huppert, H. E. & Sparks, R. J. (1990). Convection and crystallisation in magma cooled from above. *Earth and Planetary Science Letters* **101**, 78–89.

Wyllie, P. J. (1963). Effects of the changes in slope occurring on liquidus and solidus paths in the system diopside–anorthite–albite. *Mineralogical Society of America Special Paper* **1**, 204–212.

Xu, Y., Shankland, T. J., Linhardt, S., Rubie, D. C., Langenhorst, F. & Klasinski, K. (2004). Thermal diffusivity and conductivity of olivine, wadsleyite and ringwoodite to 20 GPa and 1373 K. *Physics of the Earth and Planetary Interiors* , **143–144**, 321–336.

APPENDIX

Density distribution of plagioclase composition

Following Rudge (2008) and Thompson & Maclennan (2013), the shape of the global distribution of plagioclase compositions (An%) in each sample was assessed in two ways that are more statistically rigorous than simple histograms.

(1) We used the Kernel density distribution (KDE; Silverman, 1986), a non-parametric method that allows estimating the probability density function (e.g. likely distribution of a random variable) of a variable (here An%). KDE is generated by summation of Gaussian functions, with standard deviation equal to the bandwidth and placed at every point in the dataset. We used an automated bandwidth calculating method (Sheather & Jones, 1991; Rudge, 2008). KDEs were calculated with the 'density' function of the 'R' statistical software package and compared with KDE calculated with the 'ksdensity' Statistics toolbook of Matlab. When the calculated bandwidth is lower than the analytical error (here defined as 1% An), we used bandwidths of 1·0. We assessed the physical significance of computed distributions using the SiZer method (Significant Zero crossings of the derivative; Chaudhuri & Marron, 1999; Rudge, 2008), which investigates how the KDE evolves with varying bandwidths and highlights peaks and troughs in the distribution based on the identification of regions with significant gradients. SiZer maps were calculated with the 'feature' package of 'R' (Duong et al., 2008).

(2) We used Gaussian Mixture Modeling (GMM) based on the assumption that the true distribution can be defined as a series of normal distributions (Fraley & Raftery, 2002). Each component defines a peak in the distribution and adding these components together approximates the overall distribution. GMM modeling was performed with the 'mclust' package of 'R' (Fraley & Raftery, 2002).

Calculation of interstitial liquid fraction in cumulate rocks

The whole-rock composition of a cumulate sample is determined by the relative contributions of the crystallized intercumulus liquid and that of the cumulus crystal matrix. For an element i, it can be expressed by the following equation:

$$c_i^{\mathrm{WR}} = X^{\mathrm{IL}} c_i^{\mathrm{Liq}} + \sum X^j c_i^j \tag{A1}$$

with

$$\sum X^j = 1 - X^{\mathrm{IL}} \tag{A2}$$

where X^{IL} is the interstitial liquid fraction, c_i^{Liq} is the concentration of element i in the liquid, X^j is the modal fraction of the cumulus phase j in the cumulate and c_i^j is the concentration of element i in phase j.

Following equation (A2), the proportion of intercumulus liquid (X^{IL}) can be determined using the concentration of an element i in the whole-rock (c^{WR}) when the concentration of i in the equilibrium melt (c^{Liq}) and in the crystal matrix ($\sum X^j c_i^j$) are estimated. The proportions of the various cumulus phases are, however, initially unknown and cannot be directly estimated from the bulk modal proportions owing to the presence of intercumulus material. We have thus determined the relative proportions of the intercumulus liquid and the different cumulus phases by least-squares linear regression of equation (A1). The bulk-rock composition (c^{WR}) of each sample, the equilibrium liquid composition (c^{Liq}) and the compositions of the cumulus phases (c^j), were used as input data. Mineral compositions used in equation (A1) were calculated for P using the liquid composition and appropriate partition coefficients.

The evolution of the P_2O_5 content in the liquid was calculated at each stage of fractionation using the Rayleigh fractionation model:

$$c_i^{\mathrm{Liq}} = c_{i,0}^{\mathrm{Liq}} f^{(D_i^{\mathrm{Bulk}} - 1)} \tag{A3}$$

where c_i^{Liq} is the concentration of element i in the liquid at each step, $c_{i,0}^{\mathrm{Liq}}$ is the concentration of element i in the liquid before each step, f is the mass fraction of each step relative to the mass of magma remaining in the chamber (F), and D_i^{Bulk} is the bulk partition coefficient of element i between the liquid and the crystal mush.

As a first approximation (iteration 1), the evolution of the liquid trace element content (c_i^{Liq}) was calculated using equation (A3) by simulating perfect adcumulus growth. Using the calculated c_i^{Liq} curve with differentiation, X^{IL} values were determined by least-squares regression of equation (A1) for each sample. Then, a second set of calculations of c^{Liq} (iteration 2) was performed by incorporating the effect of the intercumulus melt (X^{IL} calculated from iteration 1) and assuming that its composition equals that of the main magma body; that is, the partition coefficients equal unity. A second series of X^{IL} values was then calculated by least-squares regression of equation (A1).